ACS Catalysis

pubs.acs.org/acscatalysis

Research Article

Insights into the Influence of CeO_2 Crystal Facet on CO_2 Hydrogenation to Methanol over Pd/CeO_2 Catalysts

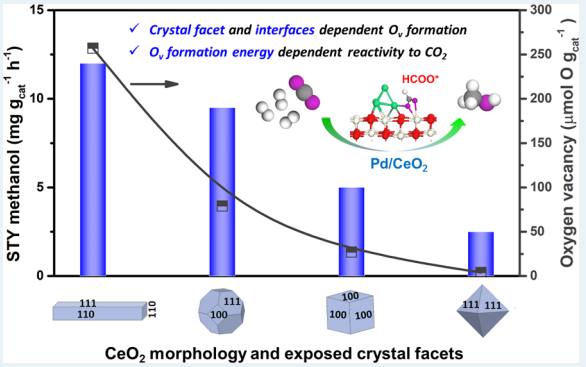
Feng Jiang, Shanshan Wang, Bing Liu, Jie Liu, Li Wang, Yang Xiao, Yuebing Xu, and Xiaohao Liu*

Cite This: *ACS Catal.* 2020, 10, 11493−11509

Read Online

ACCESS | Metrics & More | Article Recommendations | Supporting Information

ABSTRACT: CeO_2 is an excellent potential material for CO_2 hydrogenation attributed to the highly tunable properties including metal−support interaction and abundant oxygen vacancy. In this work, four CeO_2 supports with structurally well-defined different shapes and crystal facets are hydrothermally prepared, and their effects on the composition of Pd species and oxygen vacancy over Pd/CeO_2 catalysts have been intensively investigated in the reduction of CO_2 to methanol. The $2Pd/CeO_2$-R (rods) shows the highest concentration and number of oxygen vacancies, where the (110) facet with high surface oxygen mobility and low oxygen vacancy formation energy is exposed over the CeO_2-R surface. The oxygen mobility at the interface of (111) and (100) facets mainly observed on $2Pd/CeO_2$-P (polyhedrons) is higher than the single (111) and (100) facets mainly observed on $2Pd/CeO_2$-O (octahedrons) and $2Pd/CeO_2$-C (cubs), respectively. The presence of Pd highly promotes the formation of oxygen vacancies by providing dissociated H atoms to facilitate the removal of surface O in ceria support under a H_2 atmosphere. Both the $Pd_xCe_{1-x}O_\delta$ solid solution dominated on CeO_2-R and the PdO species dominated on CeO_2-O are reduced to metallic Pd after reduction with 6−10 nm average particle size. As revealed by density functional theory (DFT) calculations, in contrast to the single Pd^0 atom on CeO_2 and the thermodynamically most unstable $Pd_xCe_{1-x}O_\delta$ solid solution, the Pd^0 nanoparticles are the most stable species under the realistic reaction conditions. The $2Pd/CeO_2$-R shows the highest catalytic activity as the abundantly available oxygen vacancies function as CO_2 adsorption and activation sites. Moreover, oxygen vacancy reactivity is correlated with its formation energy. The lower formation energy facilitates the formation of oxygen vacancy; however, the reactivity of each oxygen vacancy is lower as the $TOF_{oxygen\ vacancy}$ of $2Pd/CeO_2$-O is 15 times as that of $2Pd/CeO_2$-R. Thus, a suitable oxygen vacancy formation energy is likely favorable for enhancing CO_2 reactivity. DFT calculations indicate that the CH_3OH formation is most probably from the formate (HCOO*) pathway via the C−O bond cleavage in H_2COOH*, with the reduction of HCOO* to HCOOH* as the rate-limiting step. These results would provide experimental and theoretical insights into the rational design of an effective catalyst for CO_2 hydrogenation.



KEYWORDS: *CO_2, crystal facet, CeO_2, morphology, oxygen vacancy, methanol synthesis*

Downloaded via PURDUE UNIV on September 24, 2020 at 18:32:41 (UTC).
See https://pubs.acs.org/sharingguidelines for options on how to legitimately share published articles.

1. INTRODUCTION

CO_2 emissions have emerged as a major concern ascribed to the negative and significant effects on global climate change.[1] CO_2 is an alternative, sustainable, and renewable carbon-containing resource; thus, utilization of CO_2 greatly helps alleviate CO_2 emissions and improves the independence on conventional sources including coal, petroleum, and natural gas.[2] Owing to the thermodynamic stability and chemical inertness of CO_2, its utilization as a single reactant is energy-demanding.[3] When a reductant, e.g., hydrogen (H_2), which can be generated by water splitting from geothermal, solar, and wind power, as well as a photovoltaic cell,[4] is cofed with CO_2, the reaction is more feasible. Therefore, the reduction (i.e., hydrogenation) of CO_2 has been applied to produce various valuable chemicals, including lower olefins, liquid fuels, aromatics, and ether/alcohol oxygenates.[5−12] Among these compounds, CO_2 hydrogenation to methanol (CH_3OH) has been widely investigated as methanol is an important chemical to produce aromatics and lower olefins and it itself can also be used as a fuel.[13−18]

The catalysts of converting CO_2 to methanol typically require two steps as follows: (1) CO_2 adsorption and activation and stabilizing the activated intermediates for further hydrogenation to methanol; and (2) dissociation of the H−H bond in H_2 and facilitating reactions with the

Received: July 30, 2020
Revised: September 9, 2020
Published: September 10, 2020

© XXXX American Chemical Society

https://dx.doi.org/10.1021/acscatal.0c03324
ACS Catal. 2020, 10, 11493−11509

activated intermediates to generate methanol instead of other byproducts such as methane (CH_4). Oxide supported metal catalysts are promising candidates for this reaction due to the favorable activation of CO_2 on oxide supports and the activation of H_2 on supported metals. Various metals (Rh, Re, Pt, Au, Pd, and Cu) and oxide supports (Nb_2O_5, Cr_2O_3, MgO, Ga_2O_3, CeO_2, TiO_2, SiO_2, ZrO_2, Al_2O_3, and ZnO) have been studied for this reaction.[13] These catalysts generally function via the formed alloy at the oxide−metal interfaces and/or the strong metal−support interaction (SMSI).[19,20] The oxide support exhibits a crucial role in governing the catalytic activity,[13,21−23] since it helps in increasing the metal dispersion, creating the support−metal interfacial sites, and modifying the surface properties via oxygen vacancy concentrations, basicity, or acidity, etc.

Known as a stable, abundant, and inexpensive rare-earth material, CeO_2 contains abundant surface oxygen vacancies, leading to its potentially promotional role for converting the CO_2 molecule.[24] In addition to the intrinsic properties of CeO_2, its morphology with different preferentially exposed crystal faces has been found to be a critical factor in a series of reactions, such as CO_2 methanation,[25,26] CO oxidation,[27] reverse water gas shift (RWGS),[28] and CH_4 combustion.[29] The origin of the ceria crystal face effect on the catalytic performance originates from the difference of the surface atomic arrangement and the electronic properties of CeO_2, which influences the oxygen vacancy formation energy.[30] In these reactions, the catalytic activity is highly correlated with the number of oxygen vacancies, especially for CO_2 methanation, in which the number of oxygen vacancies is linearly correlated with activity. The oxygen vacancies at the CeO_2 surface function as CO_2 adsorption and activation sites. Density functional theory (DFT) calculations reveal that CO_2 can readily be adsorbed on the CeO_2(110) surface, and the surface carbonate is formed near the oxygen vacancy site.[31] Moreover, the number of oxygen vacancies could influence CO_2 activation via lower reaction barriers of CO_2 dissociation on a divacancy as compared with a single isolated oxygen vacancy over the CeO_2(110) plane.[32] Nevertheless, the reactivity of oxygen vacancy on different crystal facets has been rarely discussed. The Pd/CeO_2 catalyst and its ability in catalyzing CO_2 to methanol have been revealed by several studies.[4,33−39] However, the crystal facet effect of the CeO_2 support is poorly understood. Therefore, a systemic investigation needs to be carried out to make a comprehensive understanding of the crystal facet effect of CeO_2 on CO_2 conversion to CH_3OH over Pd/CeO_2 catalysts.

Considering that the crystal facet of CeO_2 is highly related to its morphologies, we have synthesized CeO_2 with four different morphologies including rods, cubes, polyhedrons, and octahedrons as the support of Pd metal. The Pd/CeO_2 catalysts exhibit remarkable dependence of catalytic activity on support morphology in CO_2 conversion to methanol. The Pd/CeO_2-R material displays the highest activity among the four catalysts, which possesses the highest density and the highest amount of oxygen vacancies, originating from Pd-promoted formation of surface oxygen vacancies and the high oxygen mobility in the (110) facet of CeO_2-R. The reactivity of each oxygen vacancy is crystal-facet-dependent as well that the oxygen vacancy with a lower formation energy is prone to giving a lower reactivity, which is contrary to the relationship between the number of oxygen vacancies and their formation energy. DFT calculations were applied to reveal the possible pathway of CH_3OH formation over the Pd/CeO_2 catalyst, which indicates a preferred methanol formation from the formate route.

2. EXPERIMENTAL SECTION

2.1. Catalyst Preparation. *2.1.1. Synthesis of CeO_2 Rods (Remarked as CeO_2-R) and Cubes (Remarked as CeO_2-C).*[40] Generally, a solution composed of 3.472 g of $Ce(NO_3)_3{\cdot}6H_2O$ (Aladdin) and 20 mL of deionized (DI) water was mixed with another solution composed of 38.4 g of NaOH and 140 mL of DI water. After the obtained solution was continually stirred for 0.5 h, it was moved to a 250 mL stainless steel autoclave with a Teflon liner, followed by being hydrothermally treated at 100 °C for 24 h to obtain CeO_2-R and at 180 °C for 24 h to obtain CeO_2-C. The precipitation was then purified by centrifugation. After it was rinsed using DI water (until pH = 7) and pure ethanol for an additional three times, the final ceria samples were obtained by drying at 80 °C for 8 h and calcining in air at 400 °C for 4 h.

2.1.2. Synthesis of CeO_2 Octahedrons (Remarked as CeO_2-O). Similar to a previous study,[26] a solution composed of 1.716 g of $Ce(NO_3)_3{\cdot}6H_2O$ and 20 mL of DI water was mixed with another solution composed of 0.015 g of Na_3PO_4 and 140 mL of DI water. After the obtained solution was continually stirred for half an hour, it was moved into a 250 mL autoclave and hydrothermally treated at 170 °C for 10 h. Finally, the formed solids were separated, dried, and calcined the same way as for CeO_2-R.

2.1.3. Preparation of Ceria Polyhedrons (CeO_2-P).[41] In a standard preparation process of CeO_2-P, 5.208 g of $Ce(NO_3)_3{\cdot}6H_2O$ and 60 mL of DI water were mixed under magnetic stirring, followed by adding 1.5 g of poly(vinyl pyrrolidone) under stirring for an additional 20 min. After a clear solution was formed, 12 mL of $N_2H_4{\cdot}H_2O$ (85%) was added slowly under stirring for 15 min. The resulting solution was then moved into the 250 mL reactor and treated at 180 °C for 12 h. Finally, the precipitation was separated, dried, and calcined using the same steps as for CeO_2-R.

2.1.4. Preparation of Pd/CeO_2 Catalysts. The CeO_2-supported Pd catalysts were prepared using an incipient wetness impregnation method as described in our previous research.[42] Particularly, the loadings of Pd metal for these catalysts were the same and designed as 2.0 wt %. The real Pd contents in these samples were analyzed by inductively coupled plasma (ICP) spectroscopy (TJA IRIS 1000), which were 1.96 wt % for $2Pd/CeO_2$-R, 1.92 wt % for $2Pd/CeO_2$-P, 1.91 wt % for $2Pd/CeO_2$-C, and 2.03 wt % for $2Pd/CeO_2$-O. All of the calcined catalysts were pressed into pills and crushed, and the 280−450 μm particles were sieved for their catalytic tests.

2.2. Catalyst Characterization. In general, the calcined samples were characterized as obtained, while the reduced catalysts were initially reduced at 500 °C in H_2 at an atmospheric pressure for 1 h and then characterized after their passivation for 2 h in 1% O_2/N_2 at room temperature. The Brunauer−Emmett−Teller (BET) surface areas of Pd/CeO_2 catalysts were tested on an automated surface area analyzer (Quantachrome Autosorb iQ) from the N_2 adsorption/desorption isotherms at −196 °C. The pretreatment of these samples was degassed at 200 °C for 4 h. Conventional powder X-ray diffraction (XRD, Bruker AXS D2 PHASER) was performed at 40 kV and 40 mA using Cu (Kα) radiation (λ = 1.5406 Å). The scan was from 5 to 90° with a speed of 3°

https://dx.doi.org/10.1021/acscatal.0c03324
ACS Catal. 2020, 10, 11493−11509

min^{-1}. Raman spectra were performed on a Renishaw Micro Raman spectrometer with an excitation laser of 532 nm. High-angle annular dark-field scanning transmission electron microscopy (HAADF-STEM) was performed on an FEITecnai G2 microscope operated at 200 kV. Scanning electron microscopy (SEM) images of the ceria octahedrons were obtained on a HITACHI S-4800 microscope. Before the measurement, the samples were treated with Au sputtering first.

The CO-diffuse reflectance infrared Fourier transform spectroscopy (DRIFTS) of the reduced sample was obtained using a Nicolet Model Nexus 670 FT-IR. A high-temperature heating chamber and a mercury−cadmium−telluride (MCT) detector were equipped, and the spectra were recorded at a resolution of 4 cm^{-1} and 64 scans. The sample was first reduced in pure H_2 at 500 °C for 1 h. After the sample was cooled to 25 °C, the adsorption gas of 0.3% CO/He (15 mL min^{-1}) was fed through the chamber for 10 min and then N_2 (20 mL min^{-1}) was purged instead of 0.3% CO/He.

In situ X-ray photoelectron spectroscopy (XPS) spectra of reduced catalysts were conducted via an EnviroESCA (SPECS) equipped with a differentially pumped energy analyzer connected to an exchangeable sample environment and a monochromatic Al Kα radiation (1486.8 eV). The sample was in situ reduced in a H_2 flow of 30 mL min^{-1} at 500 °C for 1 h to obtain the XPS data for the reduced sample. The XPS spectra of calcined samples were recorded as obtained on an X-ray photoelectron spectrometer of Thermo Fisher ESCALAB 250xi. The carbonaceous C 1s peak at 284.8 eV was used to calibrate the binding energies.

H_2 temperature-programmed reduction (H_2-TPR) profiles of Pd/CeO_2 and CeO_2 supports were recorded in an auto-controlled flow reactor system (TP-5076). The sample of 50 mg was put into a tube reactor of quartz followed by a pretreatment at 200 °C for 1 h in a N_2 stream and then cooling to 30 °C. Then, it was heated from 30 to 700 °C at a ramping rate of 10 °C min^{-1} in a flow of 5%H_2/N_2. At the same time, the thermal conductivity detector (TCD) signals were recorded to get the H_2-TPR profiles.

The oxygen storage capacity (OSC) tests were carried out to quantitatively determine the density and amount of surface oxygen vacancies of these Pd/CeO_2 catalysts using an oxygen pulse injection method. First, 150 mg of the sample was dried at 200 °C for 1 h in a He stream, and then, it was reduced in 10%H_2/Ar flow at 500 °C for 1 h. The flow rate of all gas streams used in this measurement was 50 mL min^{-1}. The surface-adsorbed H_2 on the sample was removed by purging He at 500 °C for 10 min. After the catalyst was cooled to 50 °C, a stream of 10%O_2/He was injected periodically into the reduced catalyst until saturation. Finally, the OSC of the catalyst was derived from the consumption of oxygen.

Dispersion of Pd (D_{Pd}) was determined using the H_2-O_2 titration method. Typically, a sample of 100 mg was pretreated and reduced as the OSC test. Then, it was cooled to room temperature followed by injecting 10%O_2/He pulses to the sample until saturation. Subsequently, H_2 chemisorption was performed by injecting 10%H_2/Ar pulses at the same temperature. The adsorption stoichiometry factor of Pd/H_2 can be assumed to be 2/3.[43] The average particle size of Pd (d_{Pd}) was calculated using the formula d_{Pd} (nm) = 1.12/D_{Pd}.[27]

2.3. Catalyst Tests. All catalyst evaluations were carried out in a stainless steel fixed-bed reactor with a diameter of 8 mm. Typically, a catalyst of 0.3 g diluted with quartz sand of 1.0 g was packed into the reactor to eliminate the temperature gradient. The catalyst was initially in situ reduced in a 30 mL min^{-1} H_2 flow at 500 °C for 1 h and atmospheric pressure. Subsequently, the reactant gas mixture of 72.7%H_2/24.3% CO_2/3%N_2 was introduced into the reactor and then the reaction pressure was raised to the designed value followed by heating the reactor to the designed reaction temperature. The standard reaction conditions are a H_2/CO_2 ratio of 3.0, 240 °C, 3 MPa, and a gas-hourly space velocity (GHSV) of 2 L g_{cat}^{-1} h^{-1}. The online gas chromatograph (Agilent GC-7820A) equipped with an autosampler and two detectors of TCD and a flame ionization detector (FID) was applied to analyze the effluent products including CO_2, H_2, CH_4, CO, CH_3OH, and higher hydrocarbons with N_2 as the internal standard substance. Reported values are given after 5 h of reaction under the steady state.

The conversion of CO_2 (X_{CO_2}) was calculated using eq 1.

$$X_{CO_2}\ (\%) = \frac{[CO_2]_{in} - [CO_2]_{out}}{[CO_2]_{in}} \times 100\% \quad (1)$$

where $[CO_2]_{out}$ and $[CO_2]_{in}$ mean the CO_2 molar concentrations in the outlet and inlet gases, respectively.

CO selectivity (S_{CO}) and CH_4 selectivity (S_{CH_4}) were calculated using eqs 2 and 3, respectively.

$$S_{CO}\ (\%) = \frac{[CO]_{out}}{[CO_2]_{in} - [CO_2]_{out}} \times 100\% \quad (2)$$

$$S_{CH_4}\ (\%) = \frac{[CH_4]_{out}}{[CO_2]_{in} - [CO_2]_{out}} \times 100\% \quad (3)$$

where $[CO]_{out}$ and $[CH_4]_{out}$ represent the molar concentrations of CO and CH_4 in the outlet gas, respectively.

CH_3OH selectivity (S_{CH_3OH}) was calculated using eq 4.

$$S_{CH_3OH}\ (\%) = \frac{[CH_3OH]_{out}}{[CH_3OH]_{out} + [CH_4]_{out}} \times (1 - S_{CO}) \times 100\% \quad (4)$$

where $[CH_3OH]_{out}$ represents the molar concentration of CH_3OH in the outlet gas.

The reaction rate (r_{CO_2}, mmol g_{cat}^{-1} h^{-1}) was calculated using eq 5.

$$r_{CO_2} = \frac{X_{CO_2} \times V_{CO_2}}{g_{catalyst}} \quad (5)$$

where X_{CO_2} is CO_2 conversion, V_{CO_2} is the molar flow rate of CO_2 (mol h^{-1}), and $g_{catalyst}$ is the grams of catalyst loaded.

The turnover frequencies, $TOF_{oxygen\ vacancy}$ (h^{-1}) and TOF_{Pd} (h^{-1}), were calculated using eqs 6 and 7.

$$TOF_{Pd}\ (h^{-1}) = \frac{X_{CO_2} \times V_{CO_2}}{g_{catalyst} \times [Pd]_{content} \times D_{Pd} \div M_{Pd}} \quad (6)$$

$$TOF_{oxygen\ vacancy}\ (h^{-1}) = \frac{X_{CO_2} \times V_{CO_2}}{g_{catalyst} \times OSC} \quad (7)$$

where X_{CO_2}, V_{CO_2}, and $g_{catalyst}$ have the same meaning as described above, $[Pd]_{content}$ is the content of Pd in the catalyst measured by ICP (wt %), D_{Pd} is the Pd dispersion based on H_2−O_2 titration, M_{Pd} is the relative atomic mass (106.4 g

https://dx.doi.org/10.1021/acscatal.0c03324
ACS Catal. 2020, 10, 11493−11509

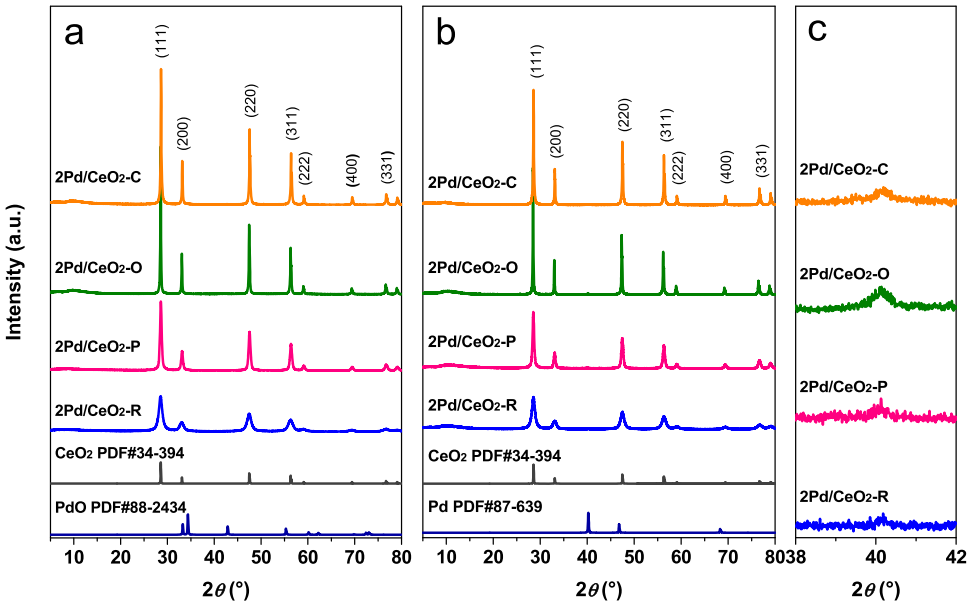


Figure 1. XRD patterns of Pd/CeO_2 catalysts for (a) calcined, (b) reduced, and (c) reflections of Pd peaks between 38 and 42°.

mol^{-1}), and OSC is the amount of surface oxygen vacancy in the catalyst (mol O g_{cat}^{-1}).

2.4. Computational Details. The Vienna ab initio simulation package (VASP) was used to carry out all of the spin-polarized DFT calculations.[44,45] A plane-wave basis was employed to describe the valence electrons. U_{eff} = 5.0 eV was applied to the Ce 4f states to accurately calculate the highly localized Ce 4f orbitals. The core−valence interactions were represented by the projector-augmented wave (PAW) method.[46] The energy cutoff was set to 400 eV. The electronic correlation and exchange was modeled by generalized gradient approximation (GGA) with the Perdew−Burke−Ernzerhof (PBE) functional.[47] The Gaussian smearing method was employed to calculate the electron smearing with a smearing width of 0.05 eV. The Brillouin zone was sampled at the Γ-point. The geometry optimization for all of the structures was performed using the conjugate gradient algorithm. The convergence criterion for force was set to 0.03 eV $Å^{-1}$. The climbing-image nudged elastic band (CI-NEB) method was used to search the transition state (TS) for each elementary reaction.[48,49] The searched transition state was further confirmed by having only one imaginary frequency. The activation barrier (E_a) was defined as the energy difference between the TS and the initial state.[50]

The calculated lattice parameter of CeO_2 was 5.437 Å. The $CeO_2(110)$ surface was modeled by a 2 × 3 supercell slab model with five layers, which contains 90 atoms. The neighboring slabs were separated by a 15 Å vacuum gap to avoid their interactions. Three-coordinated O atoms and six-coordinated Ce atoms were exposed on $CeO_2(110)$. During geometry optimization, the atoms in the bottom layer were fixed, while the rest of the atoms were allowed to relax. The CeO_2-supported Pd catalyst was modeled through adding a Pd_4 cluster on the top of the $CeO_2(110)$ surface. The side and top views of $Pd_4/CeO_2(110)$ are shown in Figure S1.

To identify the most stable Pd structure under realistic reaction conditions, we carried out ab initio thermodynamics calculations. The chemical potential of the Pd_1-CeO_2 system (μ(system)), as a function of the O chemical potential, was calculated to evaluate the stability of Pd_1-doped CeO_2 and Pd_1 supported on CeO_2, which was calculated according to eqs 8 and 9.[51]

$$\mu(\text{system}) = E_{\text{Pd}_1\text{CeO}_2} + N(\text{CeO}_2)\mu_{\text{CeO}_2}(T, P) - N(\text{O})\mu_{\text{O}}(T, P) - E_{\text{Pd}_1} - E_{\text{CeO}_2} \quad (8)$$

$$\mu_{\text{O}}(T, P) = \frac{1}{2}[E_{\text{O}_2} + \Delta\mu_{\text{O}_2}(T, P)] = \frac{1}{2}E_{\text{O}_2} + \Delta\mu_{\text{O}}(T, P) \quad (9)$$

where $E_{\text{Pd}_1\text{CeO}_2}$ is the total energy of the Pd_1CeO_2 system, E_{CeO_2} is the total energy of the bare CeO_2 surface, and E_{Pd_1} is the total energy of the bulk Pd atom. The $\mu_{\text{CeO}_2}(T, P)$ and $\mu_{\text{O}}(T, P)$ represent the chemical potentials of the bulk CeO_2 and the oxygen atom, respectively. The N values are set to balance the stoichiometry relative to a standard Pd_1CeO_2 system, namely, the CeO_2 slab surface and the bulk Pd. E_{O_2} is the total energy of the gas-phase O_2 molecule, and $\Delta\mu_{\text{O}}(T, P)$ is the free energy contribution to $\mu_{\text{O}}(T, P)$.

The chemical potential of oxygen is related to the gas-phase reservoirs.[52] Thus, for catalysts under reaction conditions, the chemical potential of oxygen was calculated using

$$\mu_{\text{O}}(T, P) = \frac{1}{4}\{3\mu_{\text{CO}_2} + 4\mu_{\text{H}_2} - \mu_{\text{CO}} - \mu_{\text{CH}_4} - \mu_{\text{CH}_3\text{OH}}\} \quad (10)$$

For catalysts under reduction conditions, the chemical potential of oxygen was calculated using

$$\mu_{\text{O}}(T, P) = \mu_{\text{H}_2\text{O}} - \mu_{\text{H}_2} \quad (11)$$

The chemical potentials for each gas species were estimated using eqs 12 and 13

$$\mu(T, P) = E + \Delta\mu(T, P) \quad (12)$$

https://dx.doi.org/10.1021/acscatal.0c03324
ACS Catal. 2020, 10, 11493−11509

Table 1. Textural Property of As-Prepared Pd/CeO_2 Samples

		grain size (nm)[a]		S_{BET} (m^2 g^{-1})[b]		lattice parameter (nm)		D_{Pd}[c]	d_{Pd} (nm)[d]
sample	exposed plane	calcined	reduced	calcined	reduced	calcined	reduced		
$2Pd/CeO_2$-R	CeO_2(110), (111)	8.8	10.1	106.3	86.3	0.5405	0.5411	0.19	5.9
$2Pd/CeO_2$-P	CeO_2(100), (111)	18.1	20.2	41.1	39.5	0.5405	0.5417	0.14	8.0
$2Pd/CeO_2$-C	CeO_2(100)	40.7	45.2	22.1	17.8	0.5394	0.5407	0.13	8.6
$2Pd/CeO_2$-O	CeO_2(111)	43.4	46.4	13.9	11.8	0.5409	0.5428	0.11	10.2

[a]Calculated by the Scherrer equation, based on the reflection of CeO_2 using the (111) peak at $2\theta = 28.6°$. [b]BET specific surface area. [c]Pd dispersion calculated by H_2-O_2 titration. [d]Average particle size of Pd calculated from Pd dispersion.

$$\Delta\mu(T, P) = [H(T, P^\theta) - H(0K, P^\theta)] - T[S(T, P^\theta) - S(0K, P^\theta)] + k_B T \ln \frac{P}{P^\theta} \quad (13)$$

where E is the DFT-calculated total energy of the gas species, P is the partial pressure of the gas species, P^θ is the standard pressure, T is the temperature of the system, k_B is the Boltzmann constant, and enthalpy $H(T, P^\theta)$ and entropy $S(T, P^\theta)$ of the gas species were obtained from the JANAF thermochemical tables.[53]

The chemical potential of Pd nanoparticles (NPs) on the ceria surface was calculated based on the Gibbs−Thomson relation.[54,55]

$$\mu_{NPs}(R) = 2\Omega\gamma_{NPs}/R \quad (14)$$

where Ω is the molar volume of the bulk Pd metal atom, R is the radius of supported Pd NPs, and γ_{NPS} is the surface energy of the Pd NPs on the ceria support. For Pd NPs on ceria, Su et al. proposed that the surface energy of Pd NPs is 0.1345 eV $Å^{-2}$, and thus the chemical potential of Pd NPs on the ceria surface is 2.69/R eV.[55]

3. RESULTS AND DISCUSSION

3.1. Structural and Morphological Study. Figure 1 illustrates the XRD patterns for the calcined and reduced Pd/CeO_2 samples. For the calcined samples (Figure 1a), each spectrum exhibits well-resolved diffraction peaks with all of the characteristic peaks located at 28.6, 33.1, 47.5, 56.3, 59.1, 69.4, and 77.0° attributed to CeO_2 crystals with the face-centered cubic structure (PDF #81-792).[56] Using the Scherrer equation and the (111) peak at $2\theta = 28.6°$, the mean crystallite sizes of CeO_2 are calculated and listed in Table 1, which are 8.8 nm for CeO_2-R, 18.1 nm for CeO_2-P, 40.7 nm for CeO_2-C, and 43.4 nm for CeO_2-O. Consequently, the CeO_2-R supported catalyst exhibits the largest surface area of 106.3 m^2 g^{-1}. No recognizable diffractions of Pd species appear in the patterns of all of the calcined samples, suggesting a highly dispersed Pd species or its incorporation into the CeO_2 lattice for the formation of the $Pd_xCe_{1-x}O_{2-\delta}$ solid solution.[57] Indeed, the XPS results in the following part clearly confirm that $Pd_xCe_{1-x}O_{2-\delta}$ is formed over the four kinds of catalysts.

For the reduced ones (Figure 1b,c), the diffraction peaks of CeO_2 are well reserved, and the diffraction peak around 40.2° assigned to metallic Pd appears due to the agglomeration of Pd species during the reduction process. However, these reflections are relatively weak, indicating the small size of Pd particles. The mean particle sizes of CeO_2 supports in these reduced catalysts are also presented in Table 1, which are slightly larger than the corresponding calcined ones owing to the sintering during the high-temperature reduction treatment. Consequently, the BET surface areas of these reduced samples are smaller than those of the corresponding calcined samples, which vary in a wide range of 11.8−86.3 m^2 g^{-1}. However, the dispersion of Pd changes in a relatively small range of 0.11−0.19 (Table 1) indicating that the unique characters of CeO_2, such as strong CeO_2−Pd interaction and rich in oxygen vacancy, could promote Pd dispersion. The mean Pd particle size could be calculated from the dispersion data, which is in the range of 6−10 nm (Table 1).

After reduction, the lattice parameters of CeO_2 are slightly increased (Table 1), which can be mainly related to the increase in the quantity of oxygen vacancies and partly due to the reduction of $Pd_xCe_{1-x}O_{2-\delta}$ during the reduction process. On the one hand, CeO_2 will be partly reduced ($2CeO_2 + H_2 \rightarrow Ce_2O_3 + H_2O$) to increase oxygen vacancies. The Ce^{3+} ions have a higher radius (r = 1.034 Å) than the Ce^{4+} ions (0.92 Å). The introduced oxygen vacancies accompanied by Ce^{3+} ions result in a distorted local symmetry, which leads to a changed length of the Ce−O bond and thereby the lattice expansion.[58,59] The reversible transformation between Ce^{3+} and Ce^{4+} is a special character of CeO_2-based catalysts, which is crucial to improve the catalytic performance. On the other hand, the Pd^{2+} ions have a similar, but slightly smaller, ionic radius (0.85 Å) as the Ce^{4+} ion, which allows the Pd ions entering the ceria lattice to form $Pd_xCe_{1-x}O_{2-\delta}$ in the calcined samples as confirmed by the XPS measurements in the following part. After reduction, Pd atoms come out of the ceria lattice, leading to an increased lattice parameter. As also revealed by the XPS results in the following part, the Pd species shows its metallic status on the catalyst surface after the reduction process.

Figure 2 represents the electron microscopy results (transmission electron microscopy (TEM) and SEM) to explore the exposed crystal facets of different shaped CeO_2 catalysts. For CeO_2-R (Figure 2a), it is composed of rods 50−150 nm in length and ∼10 nm in diameter. The interplanar spacings observed in CeO_2-R are 0.19 and 0.31 nm, indicating the presence of (110) and (111) lattice fringes, respectively (Figure 2b).[60] Figure 2c reveals that CeO_2-P is made up of polyhedrons with size of about 20 nm, and (100) and (111) lattice fringes can be observed with clear interplanar spacings of 0.27 and 0.31 nm, respectively (Figure 2d).[61] Figure 2e displays that CeO_2-C is made up of cubes with a size of about 40 nm, which is a selectively exposed (100) facet (Figure 2f). For CeO_2-O (Figure 2g), the particles are made up of octahedrons with well-defined surfaces and with lengths of 40−60 nm, which is a selectively exposed (111) facet assigned to the most thermodynamically stable crystal facet (Figure 2h). As summarized in Table 1, CeO_2-R exhibits (110) and (111) facets, while CeO_2-P exhibits (111) and (100) facets. The CeO_2-C and CeO_2-O only exhibit on single facets of (100) and (111), respectively.

https://dx.doi.org/10.1021/acscatal.0c03324
ACS Catal. 2020, 10, 11493−11509

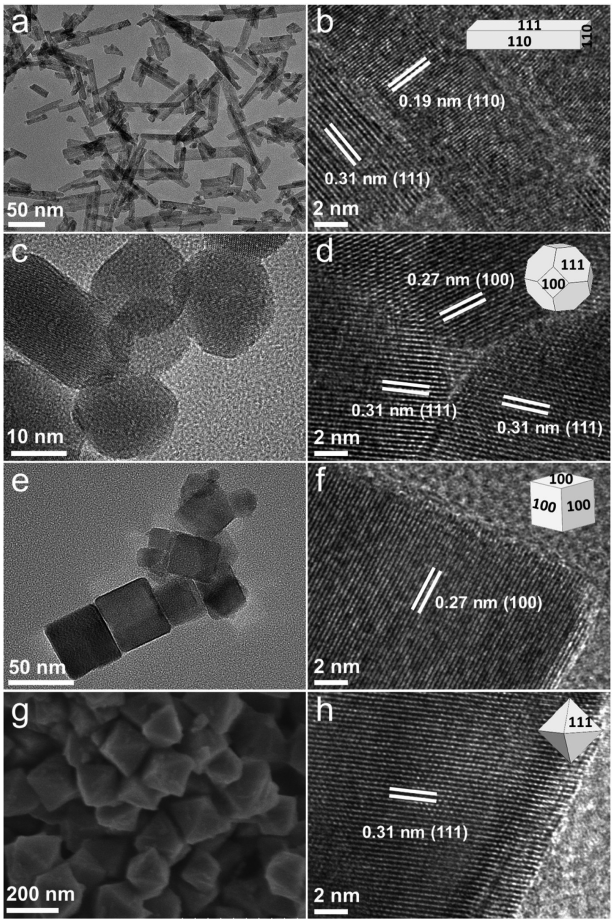


Figure 2. TEM and high-resolution TEM (HRTEM) images of CeO_2-R (a, b), CeO_2-P (c, d), and CeO_2-C (e, f). (g, h) SEM and HRTEM images of CeO_2-O. The insets schematically illustrate the crystal planes exposed on the CeO_2-R, CeO_2-P, CeO_2-C, and CeO_2-O.

The HAADF-STEM scans and energy-dispersive X-ray spectrometry (EDX) elemental mappings are used to reveal the presence of Pd species and its spatial distribution on both calcined and reduced samples (Figures S2 and 3). As shown in Figure 3, the morphologies of these supports are well reserved on the reduced catalysts. Compared with the corresponding calcined samples (Figure S2), obvious agglomeration of Pd species occurs and Pd clusters can be observed in all reduced samples except for the CeO_2-R supported one. The agglomeration of Pd species can also be deduced from the decreased surface Pd concentration and the decreased Pd/Ce ratio after the reduction process, as shown by the XPS results. Besides, Pd nanoparticles with 4−14 nm can be observed on the ceria surface, and the lattice fringe is 0.23 nm, belonging to the Pd(111) facet (Figure S3). It should be noted that Figure S3 displays not the mean size of Pd particles but the size of one particle. We intended to make the size distribution of Pd particles from TEM images. However, only the distribution of 2Pd/CeO_2-O can be obtained, attributed to the fact that it is difficult to distinguish Pd species from Ce species for the remaining three samples. On CeO_2-O, most Pd particles locate at the edges of CeO_2-O with a large average Pd particle size of 9.7 nm (Figure S4), which is similar to the Pd particle size (10.2 nm, Table 1) derived from Pd dispersion.

To further investigate the chemical states and Pd dispersion on the reduced samples, CO adsorption on the H_2-reduced samples was followed by DRIFTS. Figure 4 shows the corresponding spectra, and the dispersion of Pd species is varied over different CeO_2 supports. In general, the bands at above 2100 cm^{-1} belong to the adsorption of CO on cationic $Pd^{\delta+}$.[62] The bands in the range of 2000−2100 cm^{-1} are ascribed to the linearly adsorbed CO on Pd(111) and the Pd corner site.[63,64] The bridged CO adsorption on step sites is generally at 1940−2000 cm^{-1}.[63] The bands in the range of 1800−1940 cm^{-1} are assigned to the threefold and bridged CO adsorption on plane sites.[63,64] For all of the catalysts, the bands attributed to cationic $Pd^{\delta+}$ are relatively weak, suggesting that most of the Pd species are metallic Pd on the reduced catalysts. For the CeO_2-R and CeO_2-P supported catalysts, three types of adsorbed CO can be observed at 2064, 1962 (1970), and 1932 cm^{-1}, which are related to the linear, compressed bridged, and isolated bridged adsorption of CO, respectively.[65] Compared with 2Pd/CeO_2-R, the proportion of linearly adsorbed CO reduces owing to the less dispersion of Pd species on 2Pd/CeO_2-P. For the remaining two catalysts, the linearly adsorbed CO disappears and the band at 1850 cm^{-1} belonging to threefold adsorbed CO emerges, which originates from the larger Pd particle cluster (above 8 nm).

The chemical states of Pd species are further investigated by XPS over both reduced and calcined samples. As illustrated in Figure 5a, all of the calcined samples display two types of Pd $3d_{5/2}$ peak at 337.8 and 336.8 eV, which are ascribed to Pd^{2+} in $Pd_xCe_{1-x}O_{2-\delta}$ and in PdO particles, respectively.[27] Based on the peak areas of these two species, the proportion of $Pd_xCe_{1-x}O_{2-\delta}$ is calculated, which is 0.84 for 2Pd/CeO_2-R, 0.77 for 2Pd/CeO_2-P, 0.48 for 2Pd/CeO_2-C, and 0.39 for 2Pd/CeO_2-O (Table S1). For the 2Pd/CeO_2-R and 2Pd/CeO_2-P samples, the $Pd_xCe_{1-x}O_{2-\delta}$ solid solution dominates on the ceria surface with the ($-Pd^{2+}-O^{2-}-Ce^{4+}-$) linkages indicating atomically dispersed Pd ions in the ceria matrix.[66] For the remaining two samples, the PdO particles are located on the support surface. It is noted that the surface concentration of Pd species and the Pd/Ce ratio are quite low over 2Pd/CeO_2-R, which also confirms the embedding of Pd atoms into the ceria matrix (Table S2). After the catalyst is reduced, in situ XPS was carried out. As illustrated in Figure 5b, all of the samples exhibit only Pd^0 species on the catalyst surface with a 335.6 eV binding energy of Pd $3d_{5/2}$.[6767] It suggests that PdO and $Pd_xCe_{1-x}O_{2-\delta}$ solid solution at the catalyst surface are reduced to metallic Pd after reduction. Moreover, the surface concentration of Pd species and the Pd/Ce ratio decrease after the reduction process (Table S2), suggesting the agglomeration of Pd species, which is consistent with the TEM results.

3.2. Characterization of Oxygen Vacancy. Considering the important role of oxygen vacancy in activating CO_2, the formation process of oxygen vacancy and its dependence on the crystal facets have been investigated in this part using XPS, Raman, and OSC characterizations. Figure 6 shows the in situ XPS spectra of Ce 3d and O 1s over the reduced catalysts. As shown in Figure 6a, the Ce 3d spectra can be resolved into 10 groups for the electron structure of Ce 3d orbitals is severely influenced by the hybridization of Ce 4f orbitals with the O 2p valence band.[68] The five peaks labeled v^0 (880.8 eV), v (882.4 eV), v′ (885.3 eV), v″ (889.0 eV), and v‴ (898.4 eV) belong to Ce $3d_{5/2}$, whereas the five peaks labeled u^0 (899.1 eV), u (900.7 eV), u′ (903.6 eV), u″ (907.3 eV), and u‴ (916.7 eV)

https://dx.doi.org/10.1021/acscatal.0c03324
ACS Catal. 2020, 10, 11493−11509

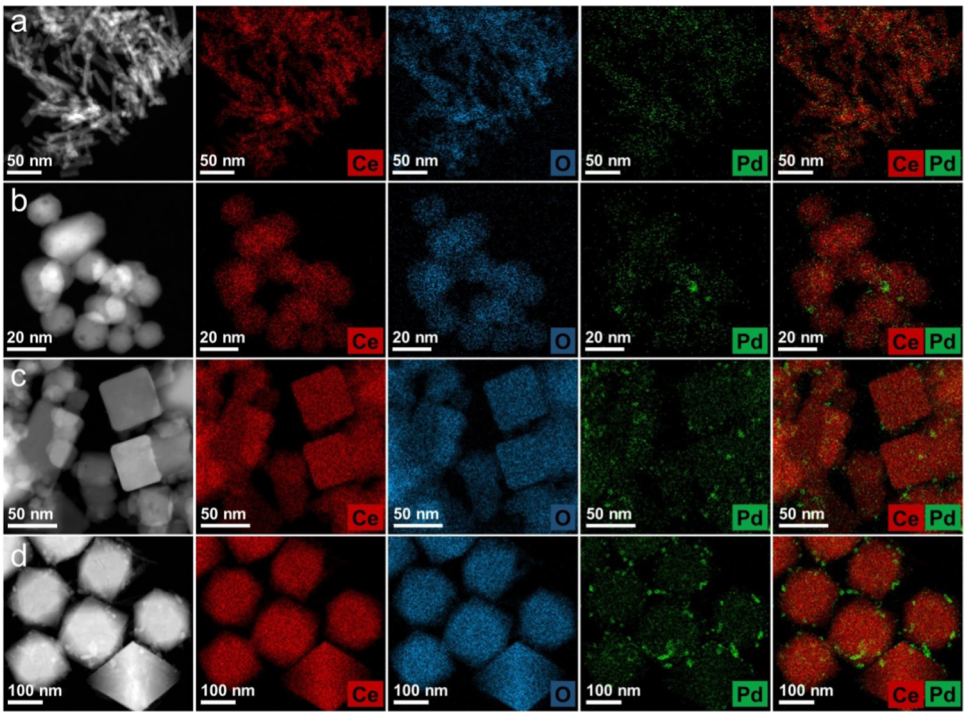


Figure 3. HAADF-STEM images and corresponding EDX elemental mappings of reduced catalysts: (a) 2Pd/CeO_2-R, (b) 2Pd/CeO_2-P, (c) 2Pd/CeO_2-C, and (d) 2Pd/CeO_2-O.

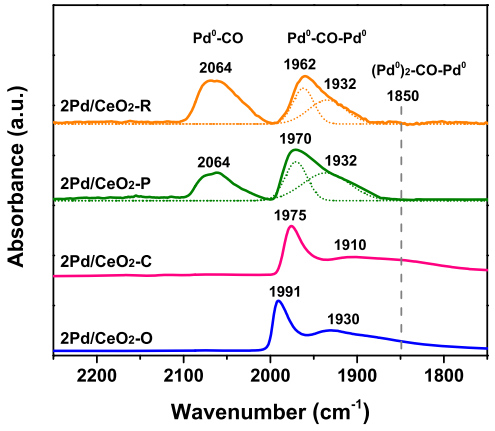


Figure 4. DRIFT spectra of CO adsorption for the reduced Pd/CeO_2 catalysts.

are assigned to Ce $3d_{3/2}$. Among the ten peaks, v^0, v′, u^0, and u′ originate from the Ce^{3+} species (Ce_2O_3), while the rest of the six peaks correspond to Ce^{4+} species (CeO_2).[27] The density of surface Ce^{3+} can be calculated by the relation $Ce^{3+}/(Ce^{3+} + Ce^{4+})$ based on Ce^{4+} and Ce^{3+} peak areas, and the results are exhibited in Table S3. The Ce^{3+} concentration can be correlated with the surface oxygen vacancies due to which the oxygen vacancy formation is always accompanied by Ce^{3+} formation. Among these catalysts, 2Pd/CeO_2-R has the highest Ce^{3+} proportion (0.49), followed by 2Pd/CeO_2-P (0.43), 2Pd/CeO_2-C (0.38), and 2Pd/CeO_2-O (0.31). The 2Pd/CeO_2-R is assumed to have the highest density of surface oxygen vacancies due to the highest Ce^{3+} density among these catalysts.

The density of oxygen vacancy on these catalysts can also be deduced from O 1s spectra. As shown in Figure 6b, three peaks can be deconvoluted from the O 1s profiles. The peak at 529.4 eV is ascribed to lattice oxygen (O_α: O^-), the peak at 531.3 eV belongs to surface oxygen (O_β: O^{2-}, O_2^{2-} or O^-), and the peak

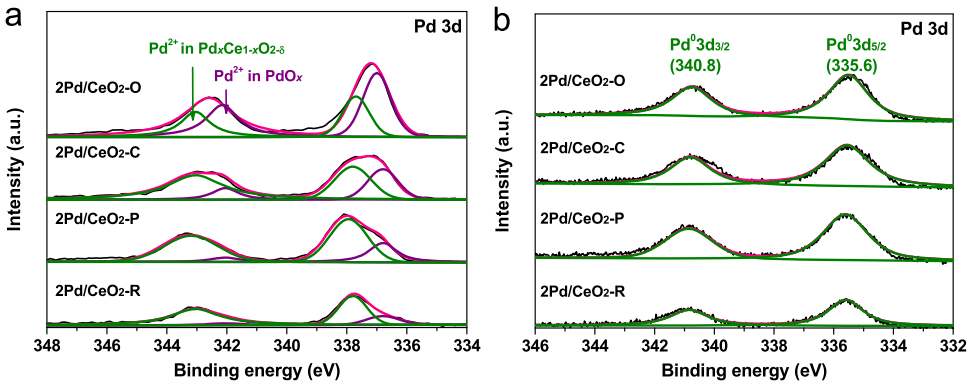


Figure 5. Pd 3d XPS curves of the (a) calcined Pd/CeO_2 catalysts and (b) in situ-reduced Pd/CeO_2 catalysts.

https://dx.doi.org/10.1021/acscatal.0c03324
ACS Catal. 2020, 10, 11493−11509

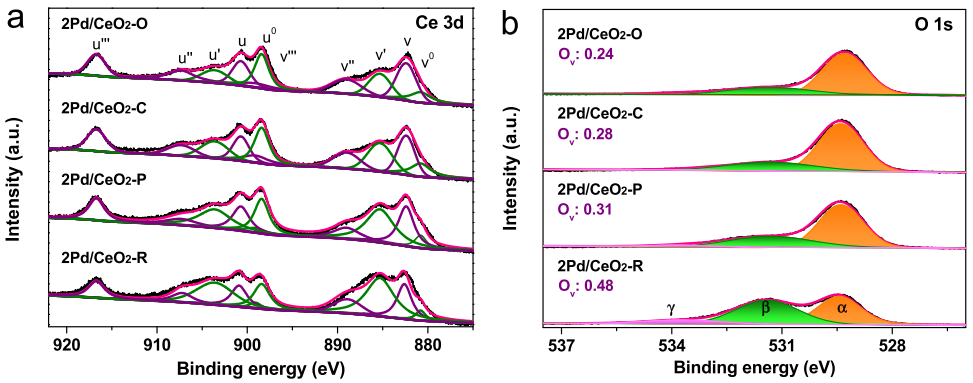


Figure 6. In situ XPS curves of (a) Ce 3d and (b) O 1s for the reduced Pd/CeO_2 catalysts.

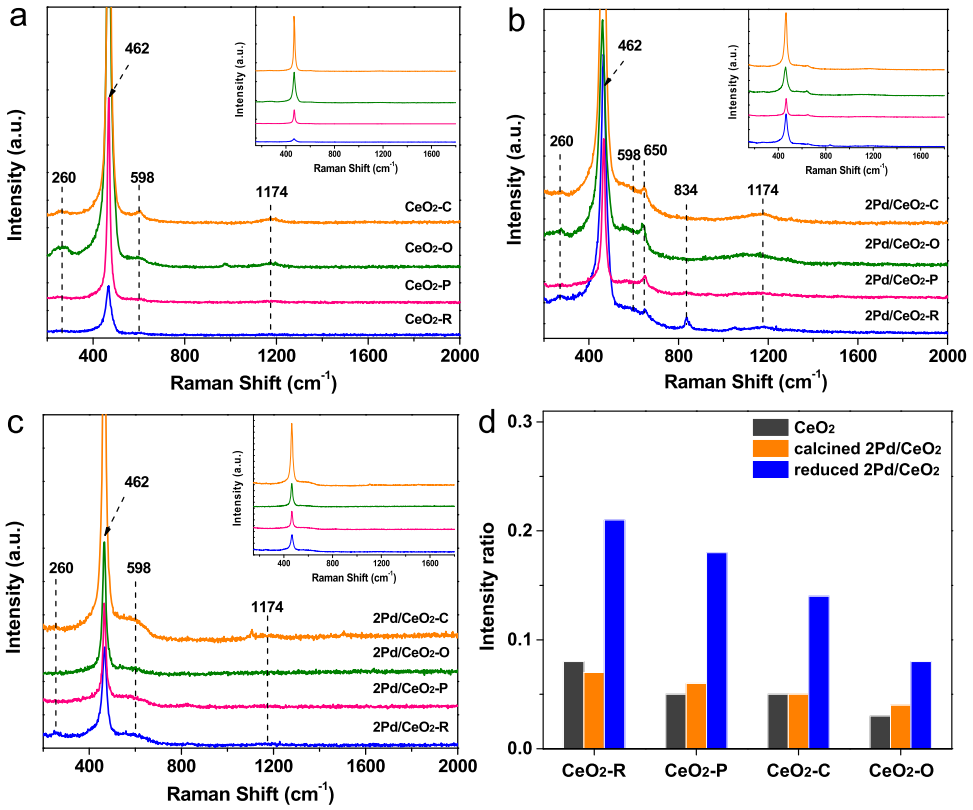


Figure 7. Raman spectra of (a) CeO_2, (b) calcined 2Pd/CeO_2, and (c) reduced 2Pd/CeO_2. (d) Corresponding I_{598}/I_{462} values.

above 532.0 eV is ascribed to other weakly bound oxygen species (O_γ) such as carbonate (CO_3^{2-}), adsorbed molecular water, and hydroxyl (OH^-).[69,70] The density of oxygen vacancies (O_v) could be assumed as $O_\beta/(O_\alpha + O_\beta + O_\gamma)$. As shown in Figure 6b and Table S4, the density of O_v ranks in the following order: 2Pd/CeO_2-R (0.48) > 2Pd/CeO_2-P (0.31) > 2Pd/CeO_2-C (0.28) > 2Pd/CeO_2-O (0.24), which is consistent with the result of the Ce 3d spectra. It suggests that the number of surface oxygen vacancies is proportional to that of Ce^{3+} sites, which can activate and transfer oxygen. We conclude that different shaped CeO_2 exposed distinct crystal facets, which thereby exhibits variation in the density of O_v.

Figure 7 illustrates Raman spectra of the pristine CeO_2, calcined, and reduced Pd/CeO_2 catalysts, respectively. All four CeO_2 supports display a strong peak at 462 nm^{-1} belonging to the vibration model of octahedral local symmetry from the CeO_2 lattice (F_{2g}), a weak defect-induced mode (D) at 598 cm^{-1}, a second-order transverse acoustic mode (2TA) at 260 cm^{-1}, and a second-order longitudinal optical (2LO) mode at 1174 cm^{-1} (Figure 7a).[60,71] The ~140 cm^{-1} difference in wavenumber is observed between F_{2g} and the defect bands, indicating that O_v of these samples arise from the intrinsic defects from Ce^{4+} to Ce^{3+}.[72] The ratio of the peak intensities at 598 and 462 cm^{-1} (I_{598}/I_{462}) is a quantitative measurement of oxygen vacancy density,[73] which decreases in the sequence below CeO_2-R (0.08) > CeO_2-P ≈ CeO_2-C (0.05) > CeO_2-O (0.03) (Figure 7d). After the loading of Pd and calcination (Figure 7b), a new peak at 650 cm^{-1} is observed in all samples. Moreover, one more new intense peak at 834 cm^{-1} is also found in the 2Pd/CeO_2-R sample. The peak at 650 cm^{-1} is assigned to Pd−O bond vibration,[74] while the peak at 834 cm^{-1} is ascribed to Pd−O−Ce bonds arising from the Pd−CeO_2 interaction.[27] This is in accordance with the XPS measurements that the PdO and $Pd_xCe_{1-x}O_{2-\delta}$ coexist on the

https://dx.doi.org/10.1021/acscatal.0c03324
ACS Catal. 2020, 10, 11493−11509

Table 2. Summary of the Raman, XPS, and OSC Results of the Reduced Pd/CeO_2 Samples

	XPS			OSC surface	
sample	$Ce^{3+}/(Ce^{4+} + Ce^{3+})$	O_v	Raman (I_{598}/I_{462})	(μmol O g_{cat}^{-1})	(μmol O m_{cat}^{-2})
2Pd/CeO_2-R	0.49	0.48	0.21	257	3.0
2Pd/CeO_2-P	0.43	0.31	0.18	79	2.0
2Pd/CeO_2-C	0.38	0.28	0.14	27	1.5
2Pd/CeO_2-O	0.31	0.24	0.08	4	0.3

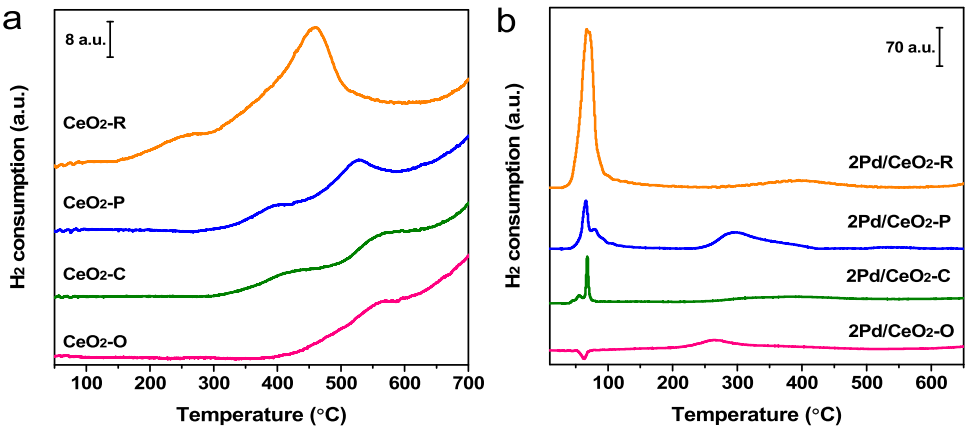


Figure 8. H_2-TPR profiles of (a) CeO_2 supports with different morphologies and (b) the corresponding calcined Pd/CeO_2 catalysts.

ceria surface for calcined catalysts and $Pd_xCe_{1-x}O_{2-\delta}$ is the dominant phase for 2Pd/CeO_2-R. Moreover, the I_{598}/I_{462} ratios of these calcined Pd/CeO_2 show no obvious change compared with the corresponding CeO_2 support (Figure 7d). As the Pd/CeO_2 samples are further reduced in the H_2 atmosphere (Figure 7c), the peaks at 650 and 834 cm^{-1} disappear, meaning the reduction of PdO species and the $Pd_xCe_{1-x}O_{2-\delta}$ solid solution, which is also consistent with the XPS results. As shown in Figure 7d, a significant increase in the I_{598}/I_{462} value occurs, suggesting that the reduction process is critical in the formation of O_v. This increase in O_v can be ascribed to the promoted partial reduction of CeO_2 to Ce_2O_3 by the hydrogen spillover from the Pd atom to the CeO_2 surface, which is also consistent with the lattice expansion as indicated by the XRD results above. The highest I_{598}/I_{462} value is obtained for 2Pd/CeO_2-R (0.21), and then 2Pd/CeO_2-P (0.18), 2Pd/CeO_2-C (0.14), and 2Pd/CeO_2-O (0.08). In summary, although the pristine CeO_2 has some oxygen vacancies, the density is relatively low. Both Pd and H_2 are crucial in promoting the partial reduction of CeO_2 to form O_v. Further, the O_v amount is highly related to the crystal facet: the 2Pd/CeO_2-R exposed (110) and (111) facets show the highest density of O_v, while the 2Pd/CeO_2-O exposed (111) facet shows the opposite. The order of O_v concentration is well in accordance with that indicated by the XPS results of O 1s and Ce 3d spectra.

The amount of surface O_v for these reduced 2Pd/CeO_2 samples is measured by OSC tests. The OSC, as well as XPS and Raman results, is summarized in Table 2. In addition to the total amount of surface O_v per gram of catalyst, the concentration of O_v per unit surface area is also calculated. It is clear that both the total amount and the concentration of O_v vary in the same order as the concentration measured by Raman and XPS. The amounts are 257, 79, 27, and 4 μmol O g_{cat}^{-1}, and the concentrations are 3.0, 2.0, 1.5, and 0.3 μmol O m_{cat}^{-2} for 2Pd/CeO_2-R, 2Pd/CeO_2-P, 2Pd/CeO_2-C, and 2Pd/CeO_2-O, respectively. The ceria-rod-supported catalyst has not only the highest density of O_v but also the highest amount of O_v attributed to its largest surface area. In general, the density of O_v highly relies on the exposed crystal facet, the existence of Pd species, and the activated atmosphere. According to the DFT calculations, the O_v formation energy increases in the order (110) < (100) < (111), which is in accordance with the sequence of the oxygen mobility of CeO_2 crystal facets.[30,75] The ceria rods exposed with (110) and (111) crystal facets have a high surface oxygen mobility and a low O_v formation energy, giving the highest O_v concentration, which is consistent with previous research.[26,27,29] The presence of Pd could effectively increase the removal of the surface O atom in the CeO_2 support under the H_2 atmosphere by the hydrogen spillover from the Pd metal to the CeO_2 support, which thereby creates more O_v. It is interesting that the 2Pd/CeO_2-P exposed (111) and (100) facets show much higher OSC than both 2Pd/CeO_2-C exposed only (100) facet and 2Pd/CeO_2-O exposed only (111) facet, which is ascribed to the fact that 2Pd/CeO_2-P has a number of interfacial sites of (100) and (111) facets and the oxygen vacancy is easier to be formed at these interfacial sites.

3.3. H_2-TPR Analysis. The reducibility of various CeO_2 supports and Pd/CeO_2 catalysts was explored using H_2-TPR (Figure 8). Figure 8a shows two types of reduction peaks in the H_2-TPR profiles of the ceria support with different morphologies. It is accepted that the reduction of surface oxygen in ceria occurs below 600 °C, and the reduction of bulk ceria generally occurs above 700 °C.[26,76] We have tried to calculate the amount of H_2 consumption over bare CeO_2 by integrating the TPR profile between 150 and 600 °C, but that of CeO_2-R can be obtained only because the H_2 consumption of the remaining samples is too low to get accurate values. It is obvious that the amount of H_2 consumption of surface oxygen decreases in the following sequence: CeO_2-R (0.36 mmol g_{cat}^{-1}) > CeO_2-P > CeO_2-C > CeO_2-O, which is in accordance with the sequence of O_v concentration as revealed by the Raman, XPS, and OSC results.

https://dx.doi.org/10.1021/acscatal.0c03324
ACS Catal. 2020, 10, 11493−11509

Table 3. Catalytic Performance of Various Pd/CeO_2 Catalysts in CO_2 Hydrogenation[a]

catalyst	r_{CO_2}		methanol STY		$TOF_{oxygen\ vacancy}$ (h^{-1})	TOF_{Pd} (h^{-1})
	mmol g_{cat}^{-1} h^{-1}	μmol m_{cat}^{-2} h^{-1}	mg g_{cat}^{-1} h^{-1}	mg m_{cat}^{-2} h^{-1}		
$2Pd/CeO_2$-R	1.3	15.1	12.0	0.14	5.1	37.0
$2Pd/CeO_2$-P	1.1	27.8	9.5	0.24	13.9	43.4
$2Pd/CeO_2$-C	0.7	39.3	5.0	0.28	25.9	29.9
$2Pd/CeO_2$-O	0.3	25.4	2.5	0.21	75.0	14.2

[a]Reaction conditions: catalyst = 0.3 g; H_2/CO_2 = 3; GHSV = 2 L g_{cat}^{-1} h^{-1}; 3 MPa; 10 h; 240 °C.

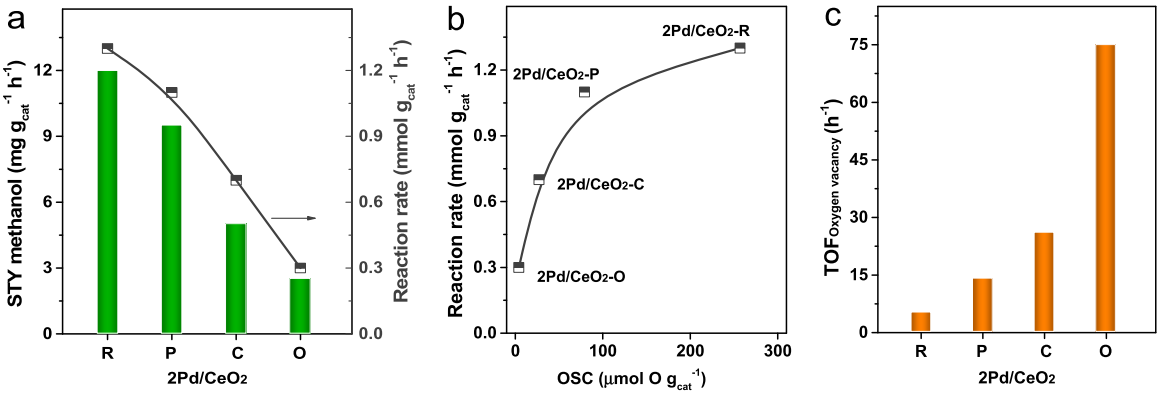


Figure 9. (a) Reaction rate and STY methanol over various Pd/CeO_2 catalysts. (b) Reaction rate as a function of the number of surface oxygen vacancies (OSCs). (c) $TOF_{oxygen\ vacancy}$ over various Pd/CeO_2 catalysts. Reaction conditions: catalyst = 0.3 g; H_2/CO_2 = 3; GHSV = 2 L g_{cat}^{-1} h^{-1}; 3 MPa; 10 h; 240 °C.

The H_2-TPR profiles of the corresponding Pd/CeO_2 catalysts are illustrated in Figure 8b, and H_2 consumption is quantitatively summarized in Table S5. For the $2Pd/CeO_2$-R catalyst, the first peak occurs at 71 °C with 1.80 mmol g_{cat}^{-1} H_2 consumption. This peak is assigned to PdO reduction as it strongly interacts with CeO_2. Notably, the amount of H_2 consumption of this peak is much bigger than that needed in reducing PdO to Pd^0 (0.19 mmol g_{cat}^{-1}). The reduction of surface oxygen over CeO_2 close to the Pd cluster is assumed to account for the additional H_2 consumption. It is noted that the values of H_2 taken up (1.80 mmol g_{cat}^{-1}) are also much bigger than the corresponding pristine CeO_2 (0.36 mmol g_{cat}^{-1}) plus reducing PdO to Pd (0.19 mmol g_{cat}^{-1}), which suggests that the presence of Pd species effectively promotes the removal of more surface oxygen species over CeO_2. For $2Pd/CeO_2$-P and $2Pd/CeO_2$-C catalysts, the two sharp peaks observed below 200 °C are ascribed to the reduction of PdO having varied interaction strengths with CeO_2. The first peak can be ascribed to the reduction of PdO with a strong interaction with CeO_2, and the second peak might originate from the reduction of PdO embedded into the CeO_2.[77] The H_2 consumption values of the two peaks are 0.35 mmol g_{cat}^{-1} for $2Pd/CeO_2$-P and 0.15 mmol g_{cat}^{-1} for $2Pd/CeO_2$-C, respectively, which are much lower than the $2Pd/CeO_2$-R catalyst. However, the $2Pd/CeO_2$-O catalyst exhibits a negative peak at 61 °C due to β-PdH decomposition.[78] The PdO species weakly interacting with the CeO_2 support is reduced to metallic Pd in the hydrogen atmosphere at room temperature, and the formed Pd can further interact with hydrogen to form β-PdH species.[79] This also indicates a lower dispersion of PdO species on the CeO_2-O support. The amount of H_2 released is only 0.03 mmol g_{cat}^{-1}, indicating that only a small amount of Pd species has a weak interaction with the CeO_2-O support. Most Pd species strongly interacting with CeO_2-O are reduced at about 262 °C. The H_2 consumption values of the peak below 200 °C per unit area are also calculated and listed in Table S5. They are 20.9, 8.9, and 8.4 μmol m_{cat}^{-2} for $2Pd/CeO_2$-R, $2Pd/CeO_2$-P, and $2Pd/CeO_2$-C, respectively. The formation of O_v is very difficult on $2Pd/CeO_2$-O, which shows no reduction of surface oxygen below 200 °C. This is consistent with the Raman, XPS, and OSC measurements. For all samples, some weak peaks are observed at 300−500 °C, which are ascribed to the reduction of surface oxygen distant from Pd clusters. In general, the loading of Pd leads to surface oxygen species reduction at lower temperatures with a higher peak area, indicating the promotional effect of Pd species on O_v formation at the ceria surface. Moreover, this promotional effect highly depends on the ceria morphology. The facile reducibility of $2Pd/CeO_2$-R is supposed to be highly related to the higher oxygen mobility in CeO_2-R.

3.4. CO_2 Hydrogenation Performances. As indicated by previous research, metal−oxide interfaces commonly play a crucial role in methanol formation from CO_2 reduction.[4,19,22] Prior to evaluating the catalytic performance of various CeO_2-supported Pd materials, the pristine four CeO_2 supports with different shapes were tested in this reaction. It turns out that all of them show negligible catalytic activity with a CO_2 conversion below 0.5%. Although the oxygen vacancies on CeO_2 supports facilitate CO_2 adsorption and activation, the CeO_2 alone cannot effectively catalyze CO_2 hydrogenation dominantly for the lack of the ability of adsorbing and activating hydrogen. Moreover, the oxygen vacancy on pristine CeO_2 could not be recycled, and their amount is also significantly less than the corresponding Pd/CeO_2 catalysts. The CO_2 hydrogenation favors proceeding by the concerted reaction between the CeO_2-activated CO_2 and Pd-activated H_2. The presence of Pd not only provides the activated hydrogen for CO_2 hydrogenation but also promotes the formation and recycling of oxygen vacancies to activate CO_2.

https://dx.doi.org/10.1021/acscatal.0c03324
ACS Catal. 2020, 10, 11493−11509

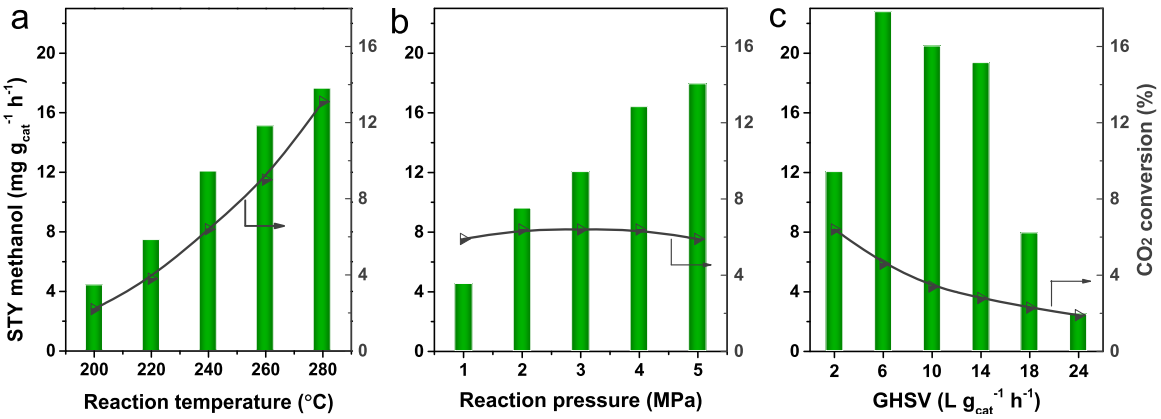


Figure 10. Influence of reaction temperature (a), reaction pressure (b), and GHSV (c) on the catalytic activity and STY methanol of the 2Pd/CeO_2-R catalyst. Standard reaction conditions: catalyst = 0.3 g; H_2/CO_2 = 3; 10 h; 3 MPa; 240 °C; GHSV = 2 L g_{cat}^{-1} h^{-1}.

As shown in Table 3 and Figure 9, the catalytic performances of the Pd/CeO_2 catalysts are highly shape-dependent. The catalytic activity is closely correlated with the CeO_2 morphology, while the product distribution is not where all of the samples show very close product selectivity (Figure S5). The CeO_2 rod supported catalyst gives the highest activity and the highest space time yield (STY) of CH_3OH among these catalysts (Figure 9a). The reaction rate of 2Pd/CeO_2-R is 1.3 mmol g_{cat}^{-1} h^{-1}, which is 1.2, 1.9, and 4.0 times of 2Pd/CeO_2-P, 2Pd/CeO_2-C, and 2Pd/CeO_2-O, respectively. The catalytic activity is supposed to be highly correlated with O_v on the catalyst surface. Generally, the activation of H_2 on Pd metal is very easy, where H_2 can dissociate spontaneously and form two adatoms on the supported Pd clusters.[80] In contrast, the activation of CO_2 is much harder and usually needs the assistance of dissociated H atoms.[19,80] Therefore, the activation of CO_2 is considered as one that decides the catalytic activity in CO_2 hydrogenation. The O_v on the ceria surface are generally accepted as the active sites for CO_2 activation. On the one hand, the oxygen vacancy can interact with nonbonding electrons from the O atoms in CO_2 via the Lewis acid−base interaction due to its Lewis acid nature.[81] On the other hand, several DFT calculations have indicated the assistance of surface O_v in CO_2 adsorption and activation.[30−32,82−85] On surface O_v, a bent CO_2^- intermediate is formed by inserting one of the two O atoms from CO_2 into the oxygen vacancy.[82] More deeply, the activation energy of CO_2 decomposition on a divacancy reduces nearly to half of that on a single isolated vacancy.[32] Thus, the higher catalytic activity over 2Pd/CeO_2-R is ascribed to the higher amount of surface O_v. As shown in Figure 9b, the increase of OSC increases the reaction rate attributed to the enhanced adsorption and activation of CO_2 on the oxygen vacancies. However, this increase is not linear and it becomes slow at higher OSC. To study the intrinsic activity of oxygen vacancies on these catalysts, the $TOF_{oxygen\ vacancy}$, which represents the converted CO_2 molecules per oxygen vacancy per hour (h^{-1}), is calculated and illustrated in Figure 9c. The $TOF_{oxygen\ vacancy}$ varies in a wide range from 5.1 to 75.0 h^{-1}, suggesting the distinctive reactivity of oxygen vacancies over different shapes of CeO_2. The 2Pd/CeO_2-R exposed (110) and (111) facets have the lowest value of $TOF_{oxygen\ vacancy}$, while the 2Pd/CeO_2-O exposed (111) facet has the highest value of $TOF_{oxygen\ vacancy}$. It seems that the easier the formation of oxygen vacancy, the less reactivity it has. The oxygen vacancy is much easier to be formed on CeO_2-R because the CeO_2(110) facet has a high oxygen mobility and low O_v formation energy. In contrast, the oxygen vacancy is much more difficult to be formed on CeO_2-O, whose exposed (111) facet has the lowest density of oxygen vacancies. This difference in the reactivity of oxygen vacancy is ascribed to the balance between vacancy filling and vacancy formation based on DFT calculations.[83] For the oxygen vacancy with a low formation energy, it is difficult to fill these vacancies using the oxygen from a source such as the highly stable CO_2. In contrast, if the energy barrier to form the oxygen vacancy is higher, filling the vacancy becomes more favorable, resulting in a stronger interaction between oxygen vacancy and CO_2.

The values of TOF_{Pd} are also calculated and presented in Table 3. The values of TOF_{Pd} are similar and around 40 h^{-1} over the CeO_2-R and CeO_2-P supported catalysts with abundant oxygen vacancies. It slightly decreases over the sample with poor oxygen vacancies, which are 29.9 and 14.2 h^{-1} over CeO_2-C and CeO_2-O supported ones, respectively. On these two samples, especially CeO_2-O, the number of oxygen vacancies highly limits the activation of CO_2. The methanol STY and the reaction rate per unit surface area have also been calculated and are listed in Table 3. They are influenced by two factors: one is the number of oxygen vacancies per unit surface area and the other is the reactivity of one single oxygen vacancy. As a result, the reaction rate and the methanol STY follow the same order of 2Pd/CeO_2-C > 2Pd/CeO_2-P > 2Pd/CeO_2-O > 2Pd/CeO_2-R.

In summary, the hydrogenation of CO_2 proceeds by the dissociation of H_2 on Pd particles and the subsequent spillover of H atoms to adsorbed and activated CO_2 on the oxygen vacancies. The activation of CO_2 is related not only to the number of oxygen vacancies but also to their reactivity. These two factors always vary in the opposite way. The 2Pd/CeO_2-R exposed (110) and (111) crystal facets exhibit the highest mobility of oxygen, but the reactivity of each oxygen vacancy is low. However, it still shows the highest reaction rate and methanol STY owing to the much higher number of oxygen vacancies than the remaining three samples.

3.5. Influence of Reaction Conditions and Catalyst Stability. The catalytic performances of the most active 2Pd/CeO_2-R catalyst are further investigated, and the influence of reaction conditions including operating temperature, reaction pressure, and GHSV is determined and illustrated in Figure 10. Both methanol STY and CO_2 conversion linearly increase with

https://dx.doi.org/10.1021/acscatal.0c03324
ACS Catal. 2020, 10, 11493−11509

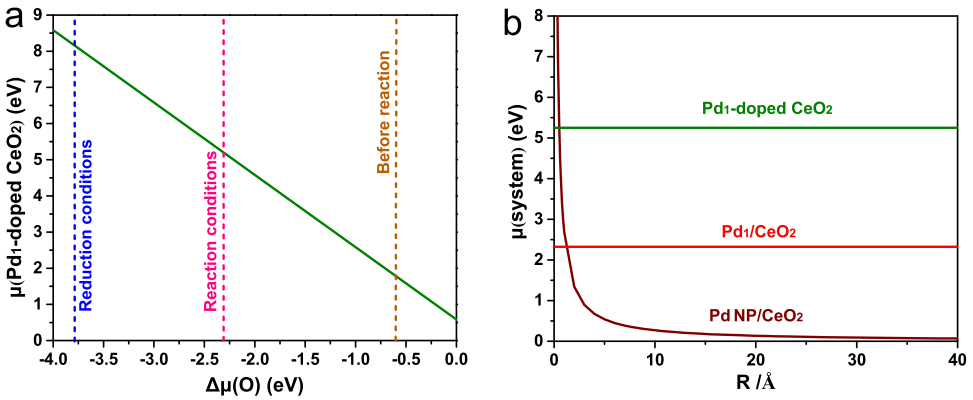


Figure 11. (a) Chemical potential of Pd_1-doped CeO_2 at different conditions. (b) Chemical potential of Pd_1-doped CeO_2 and Pd_1 supported on CeO_2 models under reaction conditions in comparison to the chemical potential of CeO_2-supported Pd metal nanoparticles (NPs) as a function of their size.

temperature increase in the range of 200−280 °C. At higher temperatures, more CO_2 molecules will be activated and subsequently converted to promote the conversion of CO_2. As we know that the production of methanol from CO_2 is exothermic (ΔH_{298K} = −49 kJ mol^{-1} for $CO_{2(g)} + 3H_{2(g)} \rightleftharpoons CH_3OH_{(g)} + H_2O_{(g)}$), while the RWGS reaction is endothermic (ΔH_{298K} = +41 kJ mol^{-1} for $CO_{2(g)} + H_{2(g)} \rightleftharpoons CO_{(g)} + H_2O_{(g)}$), higher temperature would lead more to the formation of CO. However, the product selectivity is slightly affected (Figure S6a), indicating the temperature insensitivity on the selectivity of this catalyst. In contrast, increasing the reaction pressure thermodynamically facilitates the formation of methanol. As listed above, the formation of methanol is a volume-reduced reaction, while RWGS is a volume-constant one. Increasing pressure would drive the reaction equilibrium toward methanol formation, while it has no influence on the equilibrium of the RWGS reaction. As shown in Figure 10b, methanol STY sharply increases as the reaction pressure increased from 1 to 5 MPa. However, the CO_2 conversion is slightly influenced probably because the concentration of reactants on the catalyst surface is not the rate-limiting step in the present reaction conditions. The increased methanol STY originates from the highly promoted selectivity to methanol by higher pressure (Figure S6b).

The influence of GHSV on the production of methanol shows a kind of volcano shape in the range of 2−24 L g_{cat}^{-1} h^{-1} (Figure 10c). With the increase of GHSV, the contact time between reactants and the catalyst reduces, leading to a decreased CO_2 conversion. The selectivity to methanol also decreases with an increase in CO selectivity (Figure S6c), which suggests that the formation of CO is quicker than the formation of methanol. As revealed by the DFT calculations in the following part, the formation of CO and methanol is via different pathways. The CO can be formed by direct CO_2 dissociation with a similar energy barrier as the formation of methanol, which however needs five steps. Thus, a longer contact time is favorable for the successive hydrogenation of CO_2 to CH_3OH, and the high space velocity is kinetically detrimental for methanol formation. Moreover, this phenomenon is not shape-dependent, where similar variations of conversion and selectivity can also be observed on the 2Pd/CeO_2-O catalyst, which exposes a totally different crystal facet of CeO_2(111) (Figure S7). The highest methanol STY of 22.8 $mg_{methanol}$ g_{cat}^{-1} h^{-1} is obtained at a GHSV of 6 L g_{cat}^{-1} h^{-1} over 2Pd/CeO_2-R. Thus, the catalyst stability is further evaluated at this high GHSV. As illustrated in Figure S8, the conversion of CO_2 is maintained at 4%, and CH_3OH selectivity does not drop during the 100 h time on stream. After the reaction, the cubic structure as well as the rod morphology of CeO_2 crystals is well reserved without the agglomeration of Pd species on them (Figure S9). The CeO_2 rod supported Pd catalyst displays excellent catalytic activity and long-time stability toward CO_2 hydrogenation to CH_3OH.

The catalytic performances of other Pd-based catalysts in CO_2 hydrogenation to CH_3OH are also summarized in Table S6. Clearly, the CH_3OH selectivity over supported Pd-only catalysts is mostly lower than 30% and the dominant product is CO. The formation of Pd alloy, such as PdZn alloy, could improve the methanol selectivity for stabilizing the key intermediate formate species, while the metallic Pd-only nanoparticles more prefer the RWGS reaction to make CO.[39,86] In our work, the methanol selectivity can be improved to a higher level of 47.7% by tuning the above-mentioned reaction conditions, and the TOF_{Pd} can reach 79.8 h^{-1}, which is the highest value for CeO_2-supported Pd-only catalysts attributed to the abundant oxygen vacancies in the Pd/CeO_2-R catalyst.

3.6. Possible Reaction Pathway Based on Experimental and DFT Calculations. To investigate the reaction pathway of methanol formation over the Pd/CeO_2-R catalyst, we carried out DFT calculations. Based on the above characterization results, most of the Pd species are reduced to metallic Pd after the reduction process and the average Pd particle size is about 5.9 nm. However, the existence of Pd_1/CeO_2 is not ensured because linearly adsorbed CO can be observed on this sample. To identify the most stable Pd structure under realistic reaction conditions, we carried out ab initio thermodynamic calculations. Figure 11a shows the chemical potential of Pd_1-doped CeO_2 at different conditions. Both the reduction and reaction conditions decrease the stability of the Pd_1-doped CeO_2 structure. It is in agreement with our XPS results that PdO clusters and $Pd_xCe_{1-x}O_{2-\delta}$ solid solution are reduced to metallic Pd upon reduction. Figure 11b shows the chemical potential of Pd_1-doped CeO_2 and Pd_1 supported on CeO_2 models under reaction conditions in comparison to the chemical potential of CeO_2-supported Pd metal nanoparticles (NPs) as a function of their size. It can be seen that Pd_1-doped CeO_2 and Pd_1 supported on CeO_2 are less stable under reaction conditions compared to ceria-supported Pd NPs, indicating that ceria-supported Pd NPs are the

https://dx.doi.org/10.1021/acscatal.0c03324
ACS Catal. 2020, 10, 11493−11509

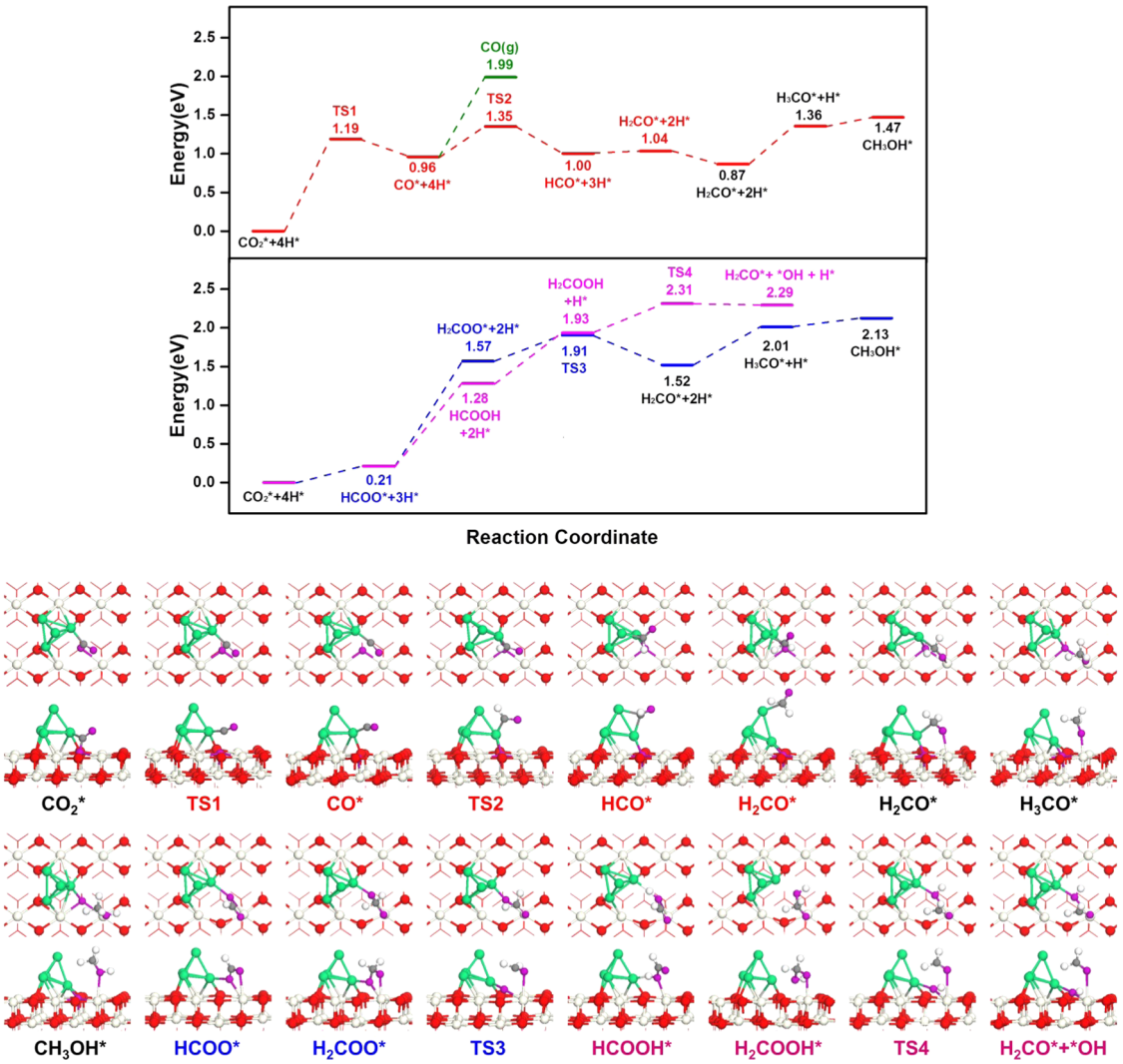


Figure 12. Calculated energy profile and intermediate structures for methanol formation on Pd/CeO_2 (110). Red, O atoms in CeO_2; ivory, Ce atoms; green, Pd atoms; gray, C atoms; purple, O atoms in CO_2; white, H atoms.

thermodynamically most favorable structure under reaction conditions. Thus, it can be inferred that Pd NPs on CeO_2 act as the active sites in the CO_2 hydrogenation reaction. Further DFT calculations on the reaction pathway were carried out using $Pd_4/CeO_2(110)$ as the model catalyst.

The reaction mechanisms of CO_2 to CH_3OH over different catalysts are supposed to be different owing to the fact that the binding of CO_2 is varied over different active sites.[24,87] The key issue in CO_2 hydrogenation to CH_3OH is breaking one of the C−O bonds. Two primary reaction pathways are proposed based on theoretical calculations and experimental observations.[19,88] One pathway is featured by the observation of the CO* intermediate, which is formed via the C−O bond cleavage in carboxylate (COOH*) species and molecularly adsorbed CO_2*. The other pathway is via a formate (HCOO*) intermediate, which is formed in the initial step of CO_2* hydrogenation, followed by several further hydrogenation steps to CH_3OH.[19] However, the occurrence of C−O bond cleavage changes from H_2COOH* to H_2COO* when the oxygen vacancies of In_2O_3 in the Pd/In_2O_3 catalyst are considered due to the stabilization of HCOO*, H_2COO*, and H_2CO* by oxygen vacancies.[80,82]

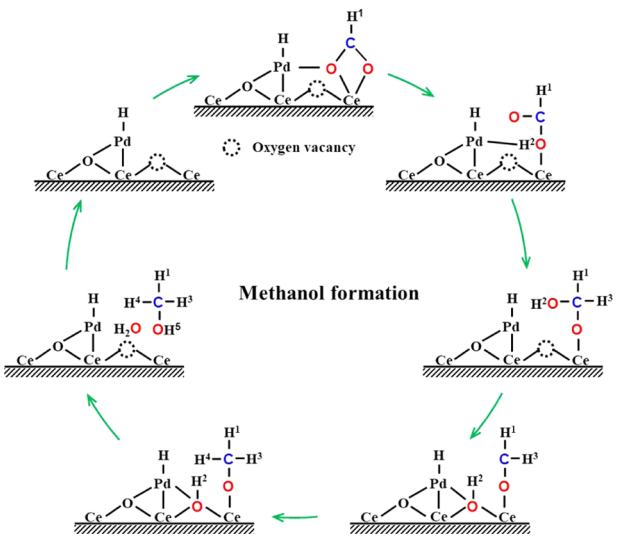
In our present work, $CeO_2(110)$ has abundant oxygen vacancies on its surface. Therefore, the activation energy of C−O bond cleavage is first calculated including the above-discussed four pathways, which are C−O bond cleavage via direct CO_2 dissociation, COOH*, H_2COOH*, and H_2COO*. Moreover, the C−O bond cleavage of HCOO* is also calculated. As shown in Figure S10, CO_2 can adsorb at the interfacial oxygen vacancy of $Pd_4/CeO_2(110)$. However, the formation of COOH* specie is difficult on the $Pd_4/CeO_2(110)$ catalyst surface. In the direct CO_2 dissociation pathway (Figure S10a), CO_2 dissociates into CO* and O*, and the dissociated O* replenishes the oxygen vacancy. This process has a barrier of 1.19 eV. For the H_2COOH* pathway (Figure S10b), 3H-assisted CO_2 dissociation with 2H binding on the C atom and one H binding on the O atom, the adsorbed CO_2 is hydrogenated to form H_2COOH* species; then, H_2COOH* species dissociates into H_2CO* and *OH. This process has a relatively low barrier of 0.38 eV. The dissociation of H_2COO* to H_2CO* has an even lower barrier of 0.34 eV (Figure S10c). In contrast, the dissociation of HCOO* to HCO* shows a much higher barrier of 1.84 eV (Figure S10d). Therefore, three C−O bond cleavage pathways of direct CO_2 dissociation and dissociation via H_2COOH* and

https://dx.doi.org/10.1021/acscatal.0c03324
ACS Catal. 2020, 10, 11493−11509

H_2COO* are considered as the potential reaction pathways of CH_3OH formation over $Pd_4/CeO_2(110)$.

Figure 12 shows the energy profiles of CH_3OH formation via the above three pathways. For the CO_2 direct dissociation route, the adsorbed CO_2 directly dissociates to CO* by overcoming a barrier of 1.19 eV. The formed CO* either desorbs (E_a = 1.03 eV) or undergoes hydrogenation to HCO* (E_a = 0.39 eV). Then, HCO* will be successively hydrogenated to H_2CO*, H_3CO*, and finally CH_3OH* as indicated by previous studies.[89,90] Among the three steps, the hydrogenation of H_2CO* to H_3CO* needs a higher energy barrier of 0.49 eV. Overall, the direct dissociation of CO_2* to CO* is the rate-determining step for CH_3OH formation. For the formate pathway via the C−O bond cleavage of CH_2OO*, the adsorbed CO_2 can be successively hydrogenated to HCOO*, H_2COO*, H_2CO*, and H_3CO* intermediates.[82] Kinetically, CO_2* hydrogenation to the HCOO* species is favorable as this reaction has a relatively small barrier of 0.21 eV. Although the barrier of C−O bond cleavage in CH_2OO* to CH_2O* is low (0.34 eV), the barrier of CH_2OO* formation is as high as 1.36 eV. For the formate pathway via the C−O bond cleavage of CH_2OOH*, CH_3OH is produced via the following sequence: CO_2*, HCOO*, HCOOH*, H_2COOH*, H_2CO*, H_3CO*, and CH_3OH*.[89,91] The bottleneck is associated with the hydrogenation of HCOO* to HCOOH*, showing a slightly lower barrier of 1.07 eV. The same rate-limiting step is also found over the ZnO/Cu(111) catalyst for CO_2 hydrogenation to methanol.[88] Therefore, CH_3OH forms likely via the formate pathway where the adsorbed CO_2 initially forms HCOO* followed by the C−O bond cleavage of the H_2COOH* intermediate (Scheme 1).

Scheme 1. Schematic Illustration of CO_2 Hydrogenation to Methanol over Pd/CeO_2 Catalysts



To further study the possibility of CO hydrogenation to CH_3OH over the Pd/CeO_2 catalyst, CO was fed and tested for temperature-programmed surface reaction (TPSR) under the same operating conditions as the real reaction except that the feeding gas of CO_2 was substituted by CO. The CO concentration was designed as 2.4%, which is the concentration assuming a 10% conversion of CO_2 to CO. As shown in Figure S11, CH_4 is the only significant product for CO hydrogenation, while no CH_3OH is generated. This observation suggests that CO may not be the intermediate for CH_3OH formation but the intermediate for CH_4 formation over the Pd/CeO_2 catalyst. Therefore, the formate route is the most possible reaction pathway for CO_2 hydrogenation to CH_3OH over the Pd/CeO_2 catalyst from both DFT and experimental results.

4. CONCLUSIONS

In conclusion, we have prepared four different morphologies of CeO_2 supports, which are rods exposing (110) and (111) facets, cubes exposing (100) facet, octahedrons exposing (111) facet, and polyhedrons exposing (111) and (100) facets. Their influences on the catalytic performance of CO_2 hydrogenation to CH_3OH have been studied. It was found that the CeO_2 morphology greatly affects the catalytic performance of Pd/CeO_2 materials owing to the character of crystal facets exposed. The main conclusions are as follows.

(1) The CeO_2 rods are mainly exposed (110) and (111) facets with the lowest oxygen vacancy formation energy and the highest density and amount of surface oxygen vacancies among these CeO_2 supports. The Pd species mainly exist as PdO clusters and $Pd_xCe_{1-x}O_\delta$ solid solution on these supports. These two types of Pd species would be reduced to metallic Pd during the reduction treatment, yielding 6−10 nm average size of Pd particles. As indicated by DFT calculations, the metallic Pd nanoparticles are the most stable species in the realistic reaction conditions compared with Pd_1/CeO_2 and $Pd_xCe_{1-x}O_\delta$ solid solution. The presence of Pd highly promotes oxygen vacancy formation via H atom spillover from the Pd surface to the CeO_2 support under a H_2 atmosphere, but it could not change the order of the concentration of oxygen vacancy, which is $2Pd/CeO_2$-R > $2Pd/CeO_2$-P > $2Pd/CeO_2$-C > $2Pd/CeO_2$-O. The oxygen mobility at the interface of (111) and (100) facets is higher than the single (111) and (100) facets.

(2) The hydrogenation of CO_2 is a synergistic reaction between H_2 adsorption/activation over the Pd surface and CO_2 adsorption/activation at the oxygen vacancy of the CeO_2 support. The catalytic activity is mainly determined by the activation of CO_2 on the oxygen vacancy on the ceria surface. The lower formation energy of oxygen vacancy could give a higher amount/concentration of oxygen vacancies, but the reactivity of one single oxygen vacancy is lower. Therefore, suitable formation energy might give superior reactivity toward CO_2. Although the reactivity of oxygen vacancy on the $2Pd/CeO_2$-R catalyst is lower, this catalyst still shows the highest catalytic activity ascribed to the much higher amount of oxygen vacancies.

(3) Combined with the DFT calculations and experimental results, the methanol formation was most probably via the formate pathway where the adsorbed CO_2 initially forms HCOO*, which is eventually hydrogenated to methanol via the C−O bond cleavage of H_2COOH* over the $Pd/CeO_2(110)$ catalyst. The gas-phase CO is not the intermediate for CH_3OH formation but the intermediate for CH_4 formation. These results would provide experimental and theoretical insights into the rational design of effective and stable catalysts for CO_2 hydrogenation.

https://dx.doi.org/10.1021/acscatal.0c03324
ACS Catal. 2020, 10, 11493−11509

■ ASSOCIATED CONTENT

Supporting Information

The Supporting Information is available free of charge at https://pubs.acs.org/doi/10.1021/acscatal.0c03324.

Structures of optimized $Pd_4/CeO_2(110)$; TEM and HRTEM images and EDX mapping for the calcined and reduced catalysts; influence of CeO_2 morphology and reaction conditions on the product distribution of these catalysts; stability test, XRD, and TEM images of the spent catalysts; calculated activation barriers for different CO_2 dissociation pathways; CO-TPSR files, binding energies, and surface compositions derived from XPS spectra; H_2 consumption derived from H_2-TPR results; summary of the Pd-based catalysts for CO_2 hydrogenation to methanol (PDF)

■ AUTHOR INFORMATION

Corresponding Author

Xiaohao Liu − *Department of Chemical Engineering, School of Chemical and Material Engineering, Jiangnan University, Wuxi 214122, China;* orcid.org/0000-0001-6746-9514; Email: liuxh@jiangnan.edu.cn

Authors

Feng Jiang − *Department of Chemical Engineering, School of Chemical and Material Engineering, Jiangnan University, Wuxi 214122, China*

Shanshan Wang − *Department of Chemical Engineering, School of Chemical and Material Engineering, Jiangnan University, Wuxi 214122, China*

Bing Liu − *Department of Chemical Engineering, School of Chemical and Material Engineering, Jiangnan University, Wuxi 214122, China*

Jie Liu − *Department of Chemical Engineering, School of Chemical and Material Engineering, Jiangnan University, Wuxi 214122, China*

Li Wang − *Department of Chemical Engineering, School of Chemical and Material Engineering, Jiangnan University, Wuxi 214122, China*

Yang Xiao − *Davidson School of Chemical Engineering, Purdue University, West Lafayette, Indiana 47907, United States;* orcid.org/0000-0003-1705-2213

Yuebing Xu − *Department of Chemical Engineering, School of Chemical and Material Engineering, Jiangnan University, Wuxi 214122, China*

Complete contact information is available at: https://pubs.acs.org/10.1021/acscatal.0c03324

Notes

The authors declare no competing financial interest.

■ ACKNOWLEDGMENTS

This work was supported by the National Natural Science Foundation of China (21706098, 21878127), the Neimenggu Key Science & Technology Plan (2019GG321), the Ordos Key Science & Technology Plan of 2019, and the Programme of Introducing Talents of Discipline to Universities (111 Project B13025). We also thank Yongkuan Wu for in situ XPS analysis, Kang Xiao for HAADF-STEM characterization, and the Central Laboratory of School of Chemical and Material Engineering of Jiangnan University for the technical assistance.

■ REFERENCES

(1) Feldman, D. R.; Collins, W. D.; Gero, P. J.; Torn, M. S.; Mlawer, E. J.; Shippert, T. R. Observational Determination of Surface Radiative Forcing by CO2 from 2000 to 2010. *Nature* **2015**, *519*, 339−343.

(2) Tackett, B. M.; Gomez, E.; Chen, J. G. Net Reduction of CO2 via Its Thermocatalytic and Electrocatalytic Transformation Reactions in Standard and Hybrid Processes. *Nat. Catal.* **2019**, *2*, 381−386.

(3) Song, C. S. Global Challenges and Strategies for Control, Conversion and Utilization of CO2 for Sustainable Development Involving Energy, Catalysis, Adsorption and Chemical Processing. *Catal. Today* **2006**, *115*, 2−32.

(4) Jiang, X.; Nie, X.; Guo, X.; Song, C.; Chen, J. G. Recent Advances in Carbon Dioxide Hydrogenation to Methanol via Heterogeneous Catalysis. *Chem. Rev.* **2020**, *120*, 7984−8034.

(5) Guo, L. S.; Sun, J.; Ge, Q. J.; Tsubaki, N. Recent Advances in Direct Catalytic Hydrogenation of Carbon Dioxide to Valuable C2+ Hydrocarbons. *J. Mater. Chem. A* **2018**, *6*, 23244−23262.

(6) Geng, S. S.; Jiang, F.; Xu, Y. B.; Liu, X. H. Iron-Based Fischer-Tropsch Synthesis for the Efficient Conversion of Carbon Dioxide into Isoparaffins. *ChemCatChem* **2016**, *8*, 1303−1307.

(7) Ma, Z. Q.; Porosoff, M. D. Development of Tandem Catalysts for CO2 Hydrogenation to Olefins. *ACS Catal.* **2019**, *9*, 2639−2656.

(8) Jiang, F.; Liu, B.; Geng, S. S.; Xu, Y. B.; Liu, X. H. Hydrogenation of CO2 into Hydrocarbons: Enhanced Catalytic Activity over Fe-Based Fischer-Tropsch Catalysts. *Catal. Sci. Technol.* **2018**, *8*, 4097−4107.

(9) Wang, W.; Wang, S. P.; Ma, X. B.; Gong, J. L. Recent Advances in Catalytic Hydrogenation of Carbon Dioxide. *Chem. Soc. Rev.* **2011**, *40*, 3703−3727.

(10) Xu, Y. B.; Shi, C. M.; Liu, B.; Wang, T.; Zheng, J.; Li, W. P.; Liu, D. P.; Liu, X. H. Selective Production of Aromatics from CO2. *Catal. Sci. Technol.* **2019**, *9*, 593−610.

(11) Liu, B.; Geng, S. S.; Zheng, J.; Jia, X. L.; Jiang, F.; Liu, X. H. Unravelling the New Roles of Na and Mn Promoter in CO2 Hydrogenation over Fe3O4-Based Catalysts for Enhanced Selectivity to Light-Olefins. *ChemCatChem* **2018**, *10*, 4718−4732.

(12) Zhou, W.; Cheng, K.; Kang, J. C.; Zhou, C.; Subramanian, V.; Zhang, Q. H.; Wang, Y. New Horizon in C1 Chemistry: Breaking the Selectivity Limitation in Transformation of Syngas and Hydrogenation of CO2 into Hydrocarbon Chemicals and Fuels. *Chem. Soc. Rev.* **2019**, *48*, 3193−3228.

(13) Li, K. Z.; Chen, J. G. G. CO2 Hydrogenation to Methanol over ZrO2-Containing Catalysts: Insights into ZrO2 Induced Synergy. *ACS Catal.* **2019**, *9*, 7840−7861.

(14) Porosoff, M. D.; Yan, B. H.; Chen, J. G. G. Catalytic Reduction of CO2 by H2 for Synthesis of CO, Methanol and Hydrocarbons: Challenges and Opportunities. *Energy Environ. Sci.* **2016**, *9*, 62−73.

(15) Wang, C. F.; Zhang, L.; Huang, X.; Zhu, Y. F.; Li, G.; Gu, Q. F.; Chen, J. Y.; Ma, L. G.; Li, X. J.; He, Q. H.; Xu, J. B.; Sun, Q.; Song, C. Q.; Peng, M.; Sun, J. L.; Ma, D. Maximizing Sinusoidal Channels of HZSM-5 for High Shape-Selectivity to P-Xylene. *Nat. Commun.* **2019**, *10*, No. 4348.

(16) Cheng, K.; Gu, B.; Liu, X. L.; Kang, J. C.; Zhang, Q. H.; Wang, Y. Direct and Highly Selective Conversion of Synthesis Gas into Lower Olefins: Design of a Bifunctional Catalyst Combining Methanol Synthesis and Carbon-Carbon Coupling. *Angew. Chem., Int. Ed.* **2016**, *55*, 4725−4728.

(17) Cheng, K.; Zhou, W.; Kang, J. C.; He, S.; Shi, S. L.; Zhang, Q. H.; Pan, Y.; Wen, W.; Wang, Y. Bifunctional Catalysts for One-Step Conversion of Syngas into Aromatics with Excellent Selectivity and Stability. *Chem* **2017**, *3*, 334−347.

(18) Zhang, P. P.; Tan, L.; Yang, G. H.; Tsubaki, N. One-Pass Selective Conversion of Syngas to Para-Xylene. *Chem. Sci.* **2017**, *8*, 7941−7946.

(19) Kattel, S.; Liu, P.; Chen, J. G. G. Tuning Selectivity of CO2 Hydrogenation Reactions at the Metal/Oxide Interface. *J. Am. Chem. Soc.* **2017**, *139*, 9739−9754.

(20) Yang, H. Y.; Zhang, C.; Gao, P.; Wang, H.; Li, X. P.; Zhong, L. S.; Wei, W.; Sun, Y. H. A Review of the Catalytic Hydrogenation of Carbon Dioxide into Value-Added Hydrocarbons. *Catal. Sci. Technol.* **2017**, *7*, 4580−4598.
(21) Vourros, A.; Garagounis, I.; Kyriakou, V.; Carabineiro, S. A. C.; Maldonado-Hodard, F. J.; Mamellos, G. E.; Konsolakis, M. Carbon Dioxide Hydrogenation over Supported Au Nanoparticles: Effect of the Support. *J. CO_2 Util.* **2017**, *19*, 247−256.
(22) Zhong, J.; Yang, X.; Wu, Z.; Liang, B.; Huang, Y.; Zhang, T. State of the Art and Perspectives in Heterogeneous Catalysis of CO2 Hydrogenation to Methanol. *Chem. Soc. Rev.* **2020**, *49*, 1385−1413.
(23) Fang, X.; Liu, B.; Cao, K.; Yang, P.; Zhao, Q.; Jiang, F.; Xu, Y.; Chen, R.; Liu, X. Particle-Size-Dependent Methane Selectivity Evolution in Cobalt-Based Fischer-Tropsch Synthesis. *ACS Catal.* **2020**, *10*, 2799−2816.
(24) Chang, K.; Zhang, H. C.; Cheng, M. J.; Lu, Q. Application of Ceria in CO2 Conversion Catalysis. *ACS Catal.* **2020**, *10*, 613−631.
(25) Wang, F.; Li, C. M.; Zhang, X. Y.; Wei, M.; Evans, D. G.; Duan, X. Catalytic Behavior of Supported Ru Nanoparticles on the {100}, {110}, and {111} Facet of CeO2. *J. Catal.* **2015**, *329*, 177−186.
(26) Sakpal, T.; Lefferts, L. Structure-Dependent Activity of CeO2 Supported Ru Catalysts for CO2 Methanation. *J. Catal.* **2018**, *367*, 171−180.
(27) Hu, Z.; Liu, X. F.; Meng, D. M.; Guo, Y.; Guo, Y. L.; Lu, G. Z. Effect of Ceria Crystal Plane on the Physicochemical and Catalytic Properties of Pd/Ceria for CO and Propane Oxidation. *ACS Catal.* **2016**, *6*, 2265−2279.
(28) Lin, L.; Yao, S.; Liu, Z.; Zhang, F.; Li, N.; Vovchok, D.; Martínez-Arias, A.; Castañeda, R.; Lin, J.; Senanayake, S. D.; Su, D.; Ma, D.; Rodriguez, J. A. In Situ Characterization of Cu/CeO2 Nanocatalysts for CO2 Hydrogenation: Morphological Effects of Nanostructured Ceria on the Catalytic Activity. *J. Phys. Chem. C* **2018**, *122*, 12934−12943.
(29) Lei, Y. Y.; Li, W. Z.; Liu, Q. C.; Lin, Q. Z.; Zheng, X. S.; Huan, Q. F.; Guan, S. N.; Wang, X. H.; Wang, C. X.; Li, F. Y. Typical Crystal Face Effects of Different Morphology Ceria on the Activity of Pd/CeO2 Catalysts for Lean Methane Combustion. *Fuel* **2018**, *233*, 10−20.
(30) Zhang, W.; Ma, X. L.; Xiao, H.; Lei, M.; Li, J. Mechanistic Investigations on Thermal Hydrogenation of CO2 to Methanol by Nanostructured CeO2(100): The Crystal-Plane Effect on Catalytic Reactivity. *J. Phys. Chem. C* **2019**, *123*, 11763−11771.
(31) Cheng, Z.; Sherman, B. J.; Lo, C. S. Carbon Dioxide Activation and Dissociation on Ceria (110): A Density Functional Theory Study. *J. Chem. Phys.* **2013**, *138*, No. 014702.
(32) Kumari, N.; Haider, M. A.; Agarwal, M.; Sinha, N.; Basu, S. Role of Reduced CeO2(110) Surface for CO2 Reduction to CO and Methanol. *J. Phys. Chem. C* **2016**, *120*, 16626−16635.
(33) Tsubaki, N.; Fujimoto, K. Promotional SMSI Effect on Supported Palladium Catalysts for Methanol Synthesis. *Top. Catal.* **2003**, *22*, 325−335.
(34) Phan, X. K.; Walmsley, J. C.; Bakhtiary-Davijany, H.; Myrstad, R.; Pfeifer, P.; Venvik, H.; Holmen, A. Pd/CeO2 Catalysts as Powder in A Fixed-Bed Reactor and as Coating in A Stacked Foil Microreactor for the Methanol Synthesis. *Catal. Today* **2016**, *273*, 25−33.
(35) Matsumura, Y.; Shen, W. J. Methanol Decomposition and Synthesis over Palladium Catalysts. *Top. Catal.* **2003**, *22*, 271−275.
(36) Shen, W. J.; Ichihashi, Y.; Ando, H.; Matsumura, Y.; Okumura, M.; Haruta, M. Effect of Reduction Temperature on Structural Properties and CO/CO2 Hydrogenation Characteristics of A Pd-CeO2 Catalyst. *Appl. Catal., A* **2001**, *217*, 231−239.
(37) Ma, Y. C.; Ge, Q. J.; Li, W. Z.; Xu, H. Y. Methanol Synthesis from Sulfur-Containing Syngas over Pd/CeO2 Catalyst. *Appl. Catal., B* **2009**, *90*, 99−104.
(38) Fan, L.; Fujimoto, K. Promotive SMSI Effect for Hydrogenation of Carbon-Dioxide to Methanol on a Pd/CeO2 Catalyst. *J. Catal.* **1994**, *150*, 217−220.
(39) Malik, A. S.; Zaman, S. F.; Al-Zahrani, A. A.; Daous, M. A.; Driss, H.; Petrov, L. A. Development of Highly Selective PdZn/CeO2 and Ca-Doped PdZn/CeO2 Catalysts for Methanol Synthesis from CO2 Hydrogenation. *Appl. Catal., A* **2018**, *560*, 42−53.
(40) Mai, H.-X.; Sun, L.-D.; Zhang, Y.-W.; Si, R.; Feng, W.; Zhang, H.-P.; Liu, H.-C.; Yan, C.-H. Shape-Selective Synthesis and Oxygen Storage Behavior of Ceria Nanopolyhedra, Nanorods, and Nanocubes. *J. Phys. Chem. B* **2005**, *109*, 24380−24385.
(41) Lu, F.; Meng, F. M.; Wang, L. N.; Luo, J. J.; Sang, Y. Morphology-Selective Synthesis Method of Nanopolyhedra and Square-Like CeO2 Nanoparticles. *Mater. Lett.* **2012**, *73*, 154−156.
(42) Jiang, F.; Cai, J.; Liu, B.; Xu, Y. B.; Liu, X. H. Particle Size Effects in the Selective Hydrogenation of Cinnamaldehyde over Supported Palladium Catalysts. *RSC Adv.* **2016**, *6*, 75541−75551.
(43) Bergeret, G.; Gallezot, P. Particle Size and Dispersion Measurements. *Handbook of Heterogeneous Catalysis*; Wiley, 2008; pp 738−765.
(44) Kresse, G.; Furthmuller, J. Efficient Iterative Schemes for Ab Initio Total-Energy Calculations Using A Plane-Wave Basis Set. *Phys. Rev. B* **1996**, *54*, 11169−11186.
(45) Kresse, G.; Furthmuller, J. Efficiency of Ab-Initio Total Energy Calculations for Metals and Semiconductors Using A Plane-Wave Basis Set. *Comput. Mater. Sci.* **1996**, *6*, 15−50.
(46) Blöchl, P. E. Projector Augmented-Wave Method. *Phys. Rev. B* **1994**, *50*, 17953−17979.
(47) Perdew, J. P.; Burke, K.; Ernzerhof, M. Generalized Gradient Approximation Made Simple. *Phys. Rev. Lett.* **1996**, *77*, 3865−3868.
(48) Henkelman, G.; Jonsson, H. Improved Tangent Estimate In the Nudged Elastic Band Method for Finding Minimum Energy Paths and Saddle Points. *J. Chem. Phys.* **2000**, *113*, 9978−9985.
(49) Henkelman, G.; Uberuaga, B. P.; Jonsson, H. A Climbing Image Nudged Elastic Band Method for Finding Saddle Points and Minimum Energy Paths. *J. Chem. Phys.* **2000**, *113*, 9901−9904.
(50) Liu, B.; Zhao, Z.; Henkelman, G.; Song, W. Y. Computational Design of a CeO2-Supported Pd-Based Bimetallic Nanorod for CO Oxidation. *J. Phys. Chem. C* **2016**, *120*, 5557−5564.
(51) Tang, Y.; Asokan, C.; Xu, M.; Graham, G. W.; Pan, X.; Christopher, P.; Li, J.; Sautet, P. Rh Single Atoms on TiO2 Dynamically Respond to Reaction Conditions by Adapting Their Site. *Nat. Commun.* **2019**, *10*, No. 4488.
(52) Zhang, M.; Wang, W.; Chen, Y. Insight of DFT and Ab Initio Atomistic Thermodynamics on the Surface Stability and Morphology of In2O3. *Appl. Surf. Sci.* **2018**, *434*, 1344−1352.
(53) Chase, M. NIST-JANAF Thermochemical Tables. *J. Phys. Chem. Ref. Data Monograph 9*; 1998.
(54) Parker, S. C.; Campbell, C. T. Kinetic Model for Sintering of Supported Metal Particles with Improved Size-Dependent Energetics and Applications to Au on TiO2 (110). *Phys. Rev. B* **2007**, *75*, No. 035430.
(55) Su, Y.-Q.; Filot, I. A. W.; Liu, J.-X.; Hensen, E. J. M. Stable Pd-Doped Ceria Structures for CH4 Activation and CO Oxidation. *ACS Catal.* **2018**, *8*, 75−80.
(56) Qi, L.; Yu, Q.; Dai, Y.; Tang, C.; Liu, L.; Zhang, H.; Gao, F.; Dong, L.; Chen, Y. Influence of Cerium Precursors on the Structure and Reducibility of Mesoporous CuO-CeO2 Catalysts for CO Oxidation. *Appl. Catal., B* **2012**, *119*−*120*, 308−320.
(57) Meng, L.; Lin, J.-J.; Pu, Z.-Y.; Luo, L.-F.; Jia, A.-P.; Huang, W.-X.; Luo, M.-F.; Lu, J.-Q. Identification of Active Sites for CO and CH4 Oxidation over PdO/Ce1-xPdxO2-δ Catalysts. *Appl. Catal., B* **2012**, *119*−*120*, 117−122.
(58) Hailstone, R. K.; DiFrancesco, A. G.; Leong, J. G.; Allston, T. D.; Reed, K. J. A Study of Lattice Expansion in CeO2 Nanoparticles by Transmission Electron Microscopy. *J. Phys. Chem. C* **2009**, *113*, 15155−15159.
(59) Deshpande, S.; Patil, S.; Kuchibhatla, S. V. N. T.; Seal, S. Size Dependency Variation in Lattice Parameter and Valency States in Nanocrystalline Cerium Oxide. *Appl. Phys. Lett.* **2005**, *87*, No. 133113.

https://dx.doi.org/10.1021/acscatal.0c03324
ACS Catal. 2020, 10, 11493−11509

(60) Huang, H.; Dai, Q.; Wang, X. Morphology Effect of Ru/CeO2 Catalysts for the Catalytic Combustion of Chlorobenzene. *Appl. Catal., B* **2014**, *158*−*159*, 96−105.
(61) Zheng, X.; Li, Y.; Zhang, L.; Shen, L.; Xiao, Y.; Zhang, Y.; Au, C.; Jiang, L. Insight Into the Effect of Morphology on Catalytic Performance of Porous CeO2 Nanocrystals for H2S Selective Oxidation. *Appl. Catal., B* **2019**, *252*, 98−110.
(62) Xu, J.; Ouyang, L. K.; Mao, W.; Yang, X. J.; Xu, X. C.; Su, J. J.; Zhuang, T. Z.; Li, H.; Han, Y. F. Operando and Kinetic Study of Low-Temperature, Lean-Burn Methane Combustion over a Pd/gamma-Al2O3 Catalyst. *ACS Catal.* **2012**, *2*, 261−269.
(63) Murata, K.; Ogura, K.; Ohyama, J.; Sawabe, K.; Yamamoto, Y.; Arai, S.; Satsuma, A. Selective Hydrogenation of Cinnamaldehyde over the Stepped and Plane Surface of Pd Nanoparticles with Controlled Morphologies by CO Chemisorption. *ACS Appl. Mater. Interfaces* **2020**, *12*, 26002−26012.
(64) Ozensoy, E.; Meier, D. C.; Goodman, D. W. Polarization Modulation Infrared Reflection Absorption Spectroscopy at Elevated Pressures: CO Adsorption on Pd(111) at Atmospheric Pressures. *J. Phys. Chem. B* **2002**, *106*, 9367−9371.
(65) Craciun, R.; Daniell, W.; Knozinger, H. The Effect of CeO2 Structure on the Activity of Supported Pd Catalysts Used for Methane Steam Reforming. *Appl. Catal., A* **2002**, *230*, 153−168.
(66) Priolkar, K. R.; Bera, P.; Sarode, P. R.; Hegde, M. S.; Emura, S.; Kumashiro, R.; Lalla, N. P. Formation of Ce1-xPdxO2-δ Solid Solution in Combustion-Synthesized Pd/CeO2 Catalyst: XRD, XPS, and EXAFS Investigation. *Chem. Mater.* **2002**, *14*, 2120−2128.
(67) Bai, S. X.; Shao, Q.; Wang, P. T.; Dai, Q. G.; Wang, X. Y.; Huang, X. Q. Highly Active and Selective Hydrogenation of CO2 to Ethanol by Ordered Pd-Cu Nanoparticles. *J. Am. Chem. Soc.* **2017**, *139*, 6827−6830.
(68) Yoo, C. J.; Lee, D. W.; Kim, M. S.; Moon, D. J.; Lee, K. Y. The Synthesis of Methanol from CO/CO2/H2 Gas over Cu/Ce1-xZrxO2 catalysts. *J. Mol. Catal. A: Chem.* **2013**, *378*, 255−262.
(69) Wang, N. F.; Li, S. Q.; Zong, Y. C.; Yao, Q. Sintering Inhibition of Flame-Made Pd/CeO2 Nanocatalyst for Low-Temperature Methane Combustion. *J. Aerosol Sci.* **2017**, *105*, 64−72.
(70) Wang, B. F.; Chen, B. X.; Sun, Y. H.; Xiao, H. L.; Xu, X. X.; Fu, M. L.; Wu, J. L.; Chen, L. M.; Ye, D. Q. Effects of Dielectric Barrier Discharge Plasma on the Catalytic Activity of Pt/CeO2 Catalysts. *Appl. Catal., B* **2018**, *238*, 328−338.
(71) Dai, Q.; Huang, H.; Zhu, Y.; Deng, W.; Bai, S.; Wang, X.; Lu, G. Catalysis Oxidation of 1,2-Dichloroethane and Ethyl Acetate over Ceria Nanocrystals with Well-Defined Crystal Planes. *Appl. Catal., B* **2012**, *117*−*118*, 360−368.
(72) Sudarsanam, P.; Hillary, B.; Mallesham, B.; Rao, B. G.; Amin, M. H.; Nafady, A.; Alsalme, A. M.; Reddy, B. M.; Bhargava, S. K. Designing CuOx Nanoparticle-Decorated CeO2 Nanocubes for Catalytic Soot Oxidation: Role of the Nanointerface in the Catalytic Performance of Heterostructured Nanomaterials. *Langmuir* **2016**, *32*, 2208−2215.
(73) Liu, L. J.; Yao, Z. J.; Deng, Y.; Gao, F.; Liu, B.; Dong, L. Morphology and Crystal-Plane Effects of Nanoscale Ceria on the Activity of CuO/CeO2 for NO Reduction by CO. *ChemCatChem* **2011**, *3*, 978−989.
(74) Meng, L.; Jia, A. P.; Lu, J. Q.; Luo, L. F.; Huang, W. X.; Luo, M. F. Synergetic Effects of PdO Species on CO Oxidation over PdO-CeO2 Catalysts. *J. Phys. Chem. C* **2011**, *115*, 19789−19796.
(75) Capdevila-Cortada, M.; Vilé, G.; Teschner, D.; Pérez-Ramírez, J.; López, N. Reactivity Descriptors for Ceria in Catalysis. *Appl. Catal., B* **2016**, *197*, 299−312.
(76) Carltonbird, M.; Eaimsumang, S.; Pongstabodee, S.; Boonyuen, S.; Smith, S. M.; Luengnaruemitchai, A. Effect of the Exposed Ceria Morphology on the Catalytic Activity of Gold/Ceria Catalysts for the Preferential Oxidation of Carbon Monoxide. *Chem. Eng. J.* **2018**, *344*, 545−555.
(77) Li, L. C.; Zhang, N. Q.; He, H.; Zhang, G. Z.; Song, L. Y.; Qiu, W. G. Shape-Controlled Synthesis of Pd Nanocrystals with Exposed {110} Facets and Their Catalytic Applications. *Catal. Today* **2019**, *327*, 28−36.
(78) López, J. M.; Gilbank, A. L.; Garcia, T.; Solsona, B.; Agouram, S.; Torrente-Murciano, L. The Prevalence of Surface Oxygen Vacancies over the Mobility of Bulk Oxygen in Nanostructured Ceria for the Total Toluene Oxidation. *Appl. Catal., B* **2015**, *174*−*175*, 403−412.
(79) Kaya, D.; Singh, D.; Kincal, S.; Uner, D. Facilitating Role of Pd For Hydrogen, Oxygen and Water Adsorption/Desorption Processes from Bulk CeO2 and CeO2/gamma-Al2O3. *Catal. Today* **2019**, *323*, 141−147.
(80) Ye, J. Y.; Liu, C. J.; Mei, D. H.; Ge, Q. F. Methanol Synthesis from CO2 Hydrogenation over a Pd4/In2O3 Model Catalyst: A Combined DFT and Kinetic Study. *J. Catal.* **2014**, *317*, 44−53.
(81) Xin, C. Y.; Hu, M. C.; Wang, K.; Wang, X. T. Significant Enhancement of Photocatalytic Reduction of CO2 with H2O over ZnO by the Formation of Basic Zinc Carbonate. *Langmuir* **2017**, *33*, 6667−6676.
(82) Ye, J. Y.; Liu, C. J.; Mei, D. H.; Ge, Q. F. Active Oxygen Vacancy Site for Methanol Synthesis from CO2 Hydrogenation on In2O3(110): A DFT Study. *ACS Catal.* **2013**, *3*, 1296−1306.
(83) Fronzi, M.; Daly, W.; Nolan, M. Reactivity of Metal Oxide Nanocluster Modified Rutile and Anatase TiO2: Oxygen Vacancy Formation and CO2 Interaction. *Appl. Catal., A* **2016**, *521*, 240−249.
(84) Lu, X. Q.; Wang, W. L.; Wei, S. X.; Guo, C.; Shao, Y.; Zhang, M. M.; Deng, Z. G.; Zhu, H. Y.; Guo, W. Y. Initial reduction of CO2 on perfect and O-defective CeO2 (111) surfaces: towards CO or COOH? *RSC Adv.* **2015**, *5*, 97528−97535.
(85) Kumari, N.; Sinha, N.; Haider, M. A.; Basu, S. CO2 Reduction to Methanol on CeO2 (110) Surface: A Density Functional Theory Study. *Electrochim. Acta* **2015**, *177*, 21−29.
(86) Bahruji, H.; Bowker, M.; Hutchings, G.; Dimitratos, N.; Wells, P.; Gibson, E.; Jones, W.; Brookes, C.; Morgan, D.; Lalev, G. Pd/ZnO Catalysts for Direct CO2 Hydrogenation to Methanol. *J. Catal.* **2016**, *343*, 133−146.
(87) Dang, S. S.; Yang, H. Y.; Gao, P.; Wang, H.; Li, X. P.; Wei, W.; Sun, Y. H. A Review of Research Progress on Heterogeneous Catalysts for Methanol Synthesis from Carbon Dioxide Hydrogenation. *Catal. Today* **2019**, *330*, 61−75.
(88) Kattel, S.; Ramirez, P. J.; Chen, J. G.; Rodriguez, J. A.; Liu, P. Active Sites for CO2 Hydrogenation to Methanol on Cu/ZnO Catalysts. *Science* **2017**, *355*, 1296−1299.
(89) Liu, C.; Liu, P. Mechanistic Study of Methanol Synthesis from CO2 and H2 on a Modified Model Mo6S8 Cluster. *ACS Catal.* **2015**, *5*, 1004−1012.
(90) Kattel, S.; Yan, B. H.; Yang, Y. X.; Chen, J. G. G.; Liu, P. Optimizing Binding Energies of Key Intermediates for CO2 Hydrogenation to Methanol over Oxide-Supported Copper. *J. Am. Chem. Soc.* **2016**, *138*, 12440−12450.
(91) Grabow, L. C.; Mavrikakis, M. Mechanism of Methanol Synthesis on Cu through CO2 and CO Hydrogenation. *ACS Catal.* **2011**, *1*, 365−384.

https://dx.doi.org/10.1021/acscatal.0c03324
ACS Catal. 2020, 10, 11493−11509